

This is the final peer-reviewed accepted manuscript of:

Johnson, N. C., L. Krishnamurthy, A. T. Wittenberg, B. Xiang, G. A. Vecchi, S. B. Kapnick, and S. Pascale, 2020: The Impact of Sea Surface Temperature Biases on North American Precipitation in a High-Resolution Climate Model. *J. Climate*, 33, 2427–2447.

The final published version is available online at: <https://doi.org/10.1175/JCLI-D-19-0417.1>

Rights / License:

The terms and conditions for the reuse of this version of the manuscript are specified in the publishing policy. For all terms of use and more information see the publisher's website.

This item was downloaded from IRIS Università di Bologna (<https://cris.unibo.it/>)

When citing, please refer to the published version.

The impact of sea surface temperature biases on North American precipitation in a high-resolution climate model

Nathaniel C. Johnson^{1,2}, Lakshmi Krishnamurthy^{1,2}, Andrew T. Wittenberg²,
Baoqiang Xiang^{2,3}, Gabriel A. Vecchi^{1,2,4}, Sarah Kapnick², and Salvatore
Pascale^{1,2,5}

¹Atmospheric and Oceanic Sciences Program, Princeton University, Princeton,
New Jersey

²National Oceanic and Atmospheric Administration/Geophysical Fluid
Dynamics Laboratory, Princeton, New Jersey

³University Corporation for Atmospheric Research, Boulder, Colorado

⁴Princeton Environmental Institute, Princeton University, Princeton, New Jersey

⁵Department of Earth System Science, Stanford University, Stanford, California

Journal of Climate

Revised November 5, 2019

Corresponding author address: Nathaniel C. Johnson, NOAA/Geophysical Fluid Dynamics Laboratory, Princeton University Forrestal Campus, 201 Forrestal Rd., Princeton, NJ 08540-6649
E-mail: Nathaniel.Johnson@noaa.gov

1
2
3
4
5
6
7
8
9
10
11
12
13
14
15
16
17
18
19
20
21
22
23
24

ABSTRACT

Positive precipitation biases over western North America have remained a pervasive problem in the current generation of coupled global climate models. These biases are substantially reduced, however, in a version of the Geophysical Fluid Dynamics Laboratory Forecast-oriented Low Ocean Resolution (FLOR) coupled climate model with systematic sea surface temperature (SST) biases artificially corrected through flux adjustment. This study examines how the SST biases in the Atlantic and Pacific Oceans contribute to the North American precipitation biases. Experiments with the FLOR model in which SST biases are removed in the Atlantic and Pacific are carried out to determine the contribution of SST errors in each basin to precipitation statistics over North America. Tropical and North Pacific SST biases have a strong impact on northern North American precipitation, while tropical Atlantic SST biases have a dominant impact on precipitation biases in southern North America, including the western United States. Most notably, negative SST biases in the tropical Atlantic in boreal winter induce an anomalously strong Aleutian low and a southward bias in the North Pacific storm track. In boreal summer, the negative SST biases induce a strengthened North Atlantic Subtropical High and Great Plains low-level jet. Each of these impacts contributes to positive annual mean precipitation biases over western North America. Both North Pacific and North Atlantic SST biases induce SST biases in remote basins through dynamical pathways, so a complete attribution of the effects of SST biases on precipitation must account for both the local and remote impacts.

25 **1. Introduction**

26 Prediction of regional precipitation changes, from intraseasonal and seasonal climate
27 forecasts to projections under global warming, remains a challenge owing to the complexity of
28 physical processes cutting across a wide range of time and spatial scales. Consequently, state-of-
29 the-art global climate models (GCMs) encounter persistent errors in simulating the temporal and
30 spatial variations of precipitation (Dai 2006; Phillips and Gleckler 2006; Liu et al. 2014; Mehran
31 et al. 2014). Pervasive and well-known biases include an unrealistic double Intertropical
32 Convergence Zone (Mechoso et al. 1995; Lin 2007), errors in the precipitation diurnal cycle
33 (Trenberth et al. 2003; Dai and Trenberth 2004), and the excessive production of light precipitation
34 (Dai 2006; Sun et al. 2006; Wilcox and Donner 2007; Stephens et al. 2010). Regional
35 climatological precipitation biases also are common. In this study, we focus on precipitation biases
36 over North America, with emphasis on the tendency for the simulation of excessive precipitation
37 in western North America (Phillips and Gleckler 2006; Sheffield et al. 2013; Liu et al. 2014;
38 Mehran et al. 2014; Pascale et al. 2015; Mejia et al. 2018). Approximately 75% of all models
39 participating in the Coupled Model Intercomparison Project phases 3 and 5 (CMIP3 and CMIP5)
40 exhibit positive precipitation biases over the western United States (Mejia et al. 2018). This bias
41 pattern incorporates an excessive amplitude of the annual cycle in the Pacific Northwest and the
42 failure to capture the transition from a U.S. West Coast precipitation maximum to a Southwest
43 minimum (Phillips and Gleckler 2006). The errors in southwestern North American precipitation
44 relate, in part, to errors in the simulation of the North American monsoon system (NAMS), which
45 features a peak in precipitation from July through September. GCMs typically simulate excessive
46 NAMS precipitation amounts and season length, with both an early onset and late retreat (Geil et
47 al. 2013; Sheffield et al. 2013).

48 Numerous sources likely share responsibility for the regional precipitation biases over
49 North America, including coarse representations of topography and errors in subgrid-scale model
50 parameterizations, like those of cloud microphysics and atmospheric convection. Common and
51 persistent patterns of sea surface temperature (SST) biases also may play an important role by
52 modifying the large-scale circulation and moisture transports. These common SST bias patterns
53 include an excessively cold and westward extended Pacific cold tongue (Mechoso et al. 1995; Li
54 and Xie 2014), warm SST biases in eastern tropical and subtropical oceans (Large and
55 Danabasoglu 2006; Richter 2015; Zuidema et al. 2016), and cold SST biases in the North Atlantic
56 and extratropical North Pacific (Wang et al. 2014; Zhang and Zhao 2014). Multiple reasons for
57 these common SST biases have been suggested, including errors in alongshore winds and resulting
58 ocean upwelling, misrepresented stratocumulus cloud decks and shortwave radiation fluxes, errors
59 in ocean eddy mixing and vertical ocean temperature gradients (Xu et al. 2014; Richter 2015;
60 Zuidema et al. 2016), and insufficient heat transport by the Atlantic meridional overturning
61 circulation (AMOC) (Wang et al. 2014; Zhang and Zhao 2014). Some SST biases may improve
62 with increasing oceanic and atmospheric resolution, but many of these biases still persist even as
63 resolution is increased to eddy-permitting and eddy-resolving scales (Delworth et al. 2012;
64 Kirtman et al., 2012; Griffies et al. 2015; Wittenberg et al. 2018; Vecchi et al. 2019; Adcroft et al.
65 2019; Held et al. 2019). Attribution of regional SST biases is complicated by the potentially strong
66 inter-basin links, as regional SST biases can induce biases in remote basins through atmospheric
67 and oceanic pathways (Xu et al. 2014; Wang et al. 2014; Zhang et al. 2014; Zhang and Zhao 2014;
68 Zuidema et al. 2016).

69 Although it is widely acknowledged that such SST biases can have important impacts on
70 the simulation of atmospheric circulation and precipitation, few studies have provided a

71 comprehensive analysis of how common SST bias patterns affect the biases in other climatological
72 features, including precipitation simulation. Several recent studies have demonstrated that Atlantic
73 and Pacific SST biases can have far-reaching impacts on temperature, precipitation, and
74 atmospheric circulation (Large and Danabasoglu 2006; Zhang et al. 2014; Zhang and Zhou 2014;
75 Xu et al. 2014; Zuidema et al. 2016), although the analysis of these SST bias effects was limited.
76 Keeley et al. (2012) performed a more targeted analysis of the effect of common North Atlantic
77 SST biases on North Atlantic and European climate, concluding that the extratropical North
78 Atlantic SST bias is a major cause of atmospheric circulation biases in the region. Zhang and Zhao
79 (2014) also demonstrated that North Atlantic SST biases may induce large-scale circulation
80 anomalies that project onto the northern annular mode, which then induce upstream climate
81 anomalies, including SST biases in the North Pacific.

82 The changes in atmospheric circulation and moisture induced by SST biases also have the
83 potential to affect the simulation of precipitation over North America. Recently, Mejia et al. (2018)
84 performed a regional climate model study to demonstrate that typical SST biases offshore
85 California and the Baja California Peninsula can explain a substantial fraction of the precipitation
86 biases in the western United States. In the present study, we take a larger-scale perspective and
87 investigate the impacts of these biases on North American climatological seasonal precipitation
88 through the analysis of simulations from a high-resolution GCM, focusing on the impacts of both
89 the Atlantic and Pacific SST biases and the interactions between the two basins. Approximate
90 removal of the SST biases over the globe and in selected Atlantic and Pacific regions results in
91 marked improvements in the simulation of North American precipitation, especially with respect
92 to the strong zonal contrast between the western and eastern U.S. Emerging themes in this study
93 include a dominant influence of Atlantic SST biases on the simulation of precipitation over the

94 U.S. and, as discussed briefly above, strong inter-basin links, whereby SST biases in the Pacific
95 Ocean induce SST and atmospheric biases in the Atlantic, and vice versa.

96

97 **2. Data and Methodology**

98

99 *a. Observational data*

100

101 We analyze observational data primarily for the purpose of evaluating model biases,
102 assessed for the 1951-2010 period. We estimate the observed climatological precipitation with the
103 University of Delaware (UD) product (Willmott and Matsuura 2001), a gridded dataset at 0.5°
104 resolution derived from station precipitation data. We assess the sensitivity of our analysis to
105 observation precipitation dataset by performing the same calculations with Global Precipitation
106 Climatology Centre (Schneider et al. 2014) and the Precipitation Construction over Land (Chen et
107 al. 2002) datasets. All conclusions are insensitive to precipitation dataset, and so all results with
108 these latter two datasets are relegated to the Supplemental Material. The climatological SST is
109 derived from the monthly Hadley Centre Sea Ice and Sea Surface Temperature (HadISST) dataset
110 (Rayner et al. 2003). For the storm track analyses, we use daily 500 hPa geopotential height and
111 monthly mean 200 hPa zonal wind from the National Centers for Environmental Prediction-
112 National Center for Atmospheric Research (NCEP/NCAR) reanalysis (Kalnay et al. 1996) for the
113 1976-2005 period. The 1976-2005 period is selected for comparison with the climate model
114 control simulation with 1990 levels of radiative forcing, in contrast with the SST and precipitation
115 bias analysis that measures against a simulation with historical levels of radiative forcing.

116

117 *b. FLOR Model and Experiments*

118

119 The GCM simulations analyzed in this study are generated by the Geophysical Fluid
120 Dynamics Laboratory (GFDL) Forecast-oriented Low Ocean Resolution (FLOR) model (Vecchi
121 et al. 2014; Wittenberg et al. 2018), a version of the Coupled Model version 2.5 (CM2.5; Delworth
122 et al. 2012) that retains high resolution in the atmosphere and land components (approximately
123 50km x 50km horizontal resolution) but has lower resolution in the ocean and sea ice components
124 (horizontal grid spacing of 1°, telescoping to 0.33° meridional spacing near the equator).
125 Quantities are exchanged between components conservatively, by first averaging from the
126 transmitting component's grid onto an "exchange grid" (which is the refined "overlay" of the two
127 participating components' grids), and then onto the receiving component's grid (Balaji et al. 2006).
128 The high atmospheric and land resolution has yielded benefits in problems ranging from
129 subseasonal (e.g., Xiang et al. 2014, 2019; Jiang et al. 2018) to seasonal prediction (Vecchi et al.
130 2014; Jia et al. 2015; Yang et al. 2015; Murakami et al. 2016; Kapnick et al. 2018) and to
131 anthropogenic climate change (Jia et al. 2016; van der Wiel et al. 2016; Pascale et al. 2017, 2018;
132 Yang et al. 2018; Vecchi et al. 2019), although high atmospheric resolution is not a panacea (e.g.,
133 Kapnick et al. 2018). The benefit to computational efficiency from the lower ocean and sea ice
134 resolution allows us to carry out an extensive array of experiments.

135 We compare the climatological precipitation characteristics in two versions of FLOR, the
136 standard free-running version and a version for which flux adjustments are applied to bring the
137 model's climatological SST in alignment with observations (FLOR-FA). Specifically, the flux
138 adjustment entails modifications to the model's momentum, enthalpy, and freshwater fluxes from
139 the atmosphere to the ocean in order to remove most of the difference between the model and

140 observational estimates of climatological SST and surface wind stress for the 1979-2012 period.
141 Additional details on the flux adjustment procedure are found in Vecchi et al. (2014). Figure 1
142 illustrates the annual climatological precipitation over North America in FLOR, FLOR-FA, and
143 observations, whereas Figure 2 illustrates the annual climatological SST biases in FLOR and
144 FLOR-FA (similar SST bias patterns are found for individual seasons). All climatology and bias
145 calculations are based on a simulation with historical estimates of radiative forcing for the 1951-
146 2010 period. Consistent with the common biases discussed in the introduction (cf., Fig. 6 of
147 Pascale et al. 2015), FLOR (Fig. 1b) fails to capture the amplitude of the observed (Fig. 1a) zonal
148 gradient in climatological precipitation and simulates excessive precipitation over western North
149 America. The climatological SST in FLOR also exhibits many of the biases discussed in the
150 introduction (cf., Fig. 1 of Richter 2015): strong negative biases in the extratropical Pacific and
151 Atlantic Oceans, an excessively cold Pacific cold tongue, and positive SST biases in eastern
152 tropical and subtropical regions near continents (Fig. 2a). FLOR-FA, in contrast, performs better
153 in simulating the sharp east-west precipitation gradient and reduces the western North American
154 precipitation bias (Fig. 1c) (this improvement is quantified in Section 3). This distinction in
155 climatological precipitation between FLOR and FLOR-FA holds for both cold and warm seasons
156 and in all observational datasets analyzed (Fig. S1). As discussed above, FLOR-FA – by
157 construction - also greatly reduces the SST biases (Fig. 2b), although the SST biases are not
158 eliminated, particularly in extratropical regions where the biases are strongest.

159 In addition to the historical radiative forcing simulations, we also conduct a set of
160 simulations with fixed radiative forcing to probe the physical processes that connect regional SST
161 biases to global precipitation biases, as outlined in Table 1. First, we analyze years 101-200 from
162 200-yr control simulations (to avoid any issues with model spin-up) with radiative forcing held

163 fixed at 1990 values (CTL and FA for the standard and flux-adjusted simulations, respectively).
164 The climatological differences in precipitation, SST, and atmospheric circulation between CTL
165 and FA are very similar to the differences in the historical forcing simulations. In order to
166 determine the roles of individual basin SST biases in the simulation of North American
167 precipitation, we next analyze a set of 100-yr SST nudging simulations with FLOR. In these
168 simulations, we nudge the SSTs over individual basins to the total time varying values in FA (FA
169 climatology plus FA anomalies) with a five-day restoring timescale. This procedure nearly
170 eliminates the SST differences with FA over individual basins while allowing free
171 ocean/atmosphere coupling in regions where SSTs are not restored. By allowing full coupling
172 outside the restoring regions, we can capture the influence of SST biases in one region on the SST
173 biases in remote regions, as discussed in the introduction. Because FA has much smaller SST
174 biases than CTL (Fig. 2), the SST restoring experiments essentially isolate the influence of SST
175 biases in individual basins on the simulated climate.

176 We focus on distinguishing the influence of SST biases in the North Pacific and North
177 Atlantic Oceans in four distinct regions (Fig. 3). In the simulation designated as TPNP, we restore
178 total SSTs in the tropical and extratropical North Pacific basin (15°S - 60°N, 120°E to South and
179 North American West Coast, TPNP domain hereafter) to FA values. Similarly, in the simulation
180 designated as TANA, we restore SSTs in the tropical and extratropical North Atlantic basin (15°S
181 - 60°N, South and North American East Coast to African and European West Coast, TANA
182 domain hereafter) to FA values. Beyond the edges of these domains away from the coastlines, we
183 apply a 10° buffer within which the restoring is linearly reduced to zero. To distinguish the role
184 of tropical versus extratropical SST biases, we conduct two additional experiments in which the

185 restoring is only applied to the tropics (15°S - 15°N) in the Pacific and Atlantic Oceans; we
186 designate these experiments as TP and TA, respectively.

187 We conduct two additional experiments with a reduced length of 50 years to investigate
188 the roles of local and non-locally induced SST biases. Climatological precipitation and
189 atmospheric circulation differences between experiments exhibit only small differences when
190 comparing 50-yr and 100-yr averages (not shown), and so we conclude that 50-yr simulations are
191 sufficient for the purposes of this study. Because SST biases in one basin can impact the biases in
192 remote regions, we wish to distinguish the influence of the local versus the remotely forced SST
193 biases. In the experiment designated as TPNP_{iso} (where “iso” stands for “isolated”), we restore
194 SSTs in the TPNP domain to the FA values, just as in TPNP, but we also restore the TANA domain
195 SSTs to CTL values. Therefore, the climatological SST differences between TPNP_{iso} and CTL are
196 confined to the tropical and extratropical North Pacific domain, and climatological SSTs are nearly
197 identical between TPNP_{iso} and CTL in all other ocean basins. Similarly, in the experiment
198 designated as TANA_{iso} we restore TANA domain SSTs to those of FA while also restoring the
199 TPNP SSTs to CTL values. The TPNP_{iso} and TANA_{iso} experiments allow us to decompose the
200 total effect of basin SST biases (CTL minus experiment) into locally and remotely forced
201 components:

$$202 \quad \text{CTL} - \text{TPNP} = (\text{CTL} - \text{TPNP}_{\text{iso}}) + (\text{TPNP}_{\text{iso}} - \text{TPNP}) \quad (1)$$

$$203 \quad \text{CTL} - \text{TANA} = (\text{CTL} - \text{TANA}_{\text{iso}}) + (\text{TANA}_{\text{iso}} - \text{TANA}). \quad (2)$$

204 The left-hand side represents the total effect and the two terms on the righthand side represent the
205 locally and remotely forced SST effects, respectively.

206

207 *c. Diagnostic Analyses*

208

209 To diagnose the impacts of FLOR’s SST biases on its atmospheric circulation and North
210 American precipitation, we calculate composite differences between the simulations described
211 above. To keep the analysis as simple as possible while also illustrating seasonality in the
212 response, we subdivide the calendar into two six-month seasons, a cold (October – March) and
213 warm season (April – September). Except for the historical bias calculations, differences express
214 how CTL compares with the experiment of interest and are calculated as CTL minus the
215 experiment. To calculate differences in the storm tracks, we identify the storm tracks by the
216 variance of the high-pass filtered 500 hPa geopotential height (z500) fields, where we use a
217 Butterworth filter to retain z500 variance with periods less than eight days.

218 To provide further insight into how the circulation and moisture changes induced by SST
219 biases impact climatological precipitation, we analyze the moisture budget differences between
220 the experiments. The climatological precipitation budget (e.g. Seager and Henderson 2013) can
221 be approximated by

$$222 \quad \bar{P} = -\frac{1}{\rho_w g} \nabla \cdot \int_0^{p_s} (\bar{\mathbf{u}}\bar{q} + \overline{\mathbf{u}'q'}) dp + \bar{E}, \quad (3)$$

223 where P is the precipitation, ρ_w is the density of water, g is the gravitational acceleration, p_s is the
224 surface pressure, \mathbf{u} is the horizontal wind vector, q is the specific humidity, and E is the surface
225 evaporation. Double overbars represent climatological seasonal means, and primes represent
226 deviations from the monthly means, which are at daily resolution in this study. Products of
227 monthly anomalies are neglected, as the monthly transient eddy convergence term is small over
228 the domain of interest (not shown). The two terms within the integral represent the effects of
229 moisture convergence from the climatological flow and the submonthly transient eddy moisture
230 flux convergence, respectively.

231 As discussed in Seager and Henderson (2013), the moisture budget calculations are quite
232 sensitive to the horizontal, vertical, and temporal resolution of the archived data, which typically
233 are stored in a standard grid that is distinct from the model's native grid. In the FLOR experiments,
234 the monthly data are saved at 17 standard vertical levels, but the relevant daily data are only
235 available at three vertical levels (surface, 850 hPa, and 500 hPa). The poor vertical resolution of
236 the higher-frequency data means that the transient eddy moisture flux convergence calculations
237 are not reliable. Nevertheless, we evaluated whether the estimates from (3) are accurate enough
238 to provide some insight about the differences in seasonal mean precipitation between the
239 experiments. Figure 4 shows the seasonal CTL minus FA precipitation differences and the
240 corresponding differences estimated by (3). The fields in Fig. 4 are smoothed through 20 iterations
241 of two-dimensional convolution with a 3 x 3 kernel, which especially reduces error in the
242 decomposition by (3) over regions of strongly varying topography. The actual and derived
243 precipitation climatology differences in Fig. 4 agree rather well over the Pacific, North America,
244 and Atlantic regions, indicating that the resolution of the archived data is enough to capture general
245 features in the precipitation budget differences. For the entire Northern Hemisphere, the pattern
246 correlations between the actual precipitation climatology difference pattern and that derived from
247 (1) are 0.89 in October-March and 0.92 in April-September, supporting the reliability of the
248 moisture budget decomposition in capturing the overall spatial differences. The quantitative
249 differences, however, are large enough that caution must be made to avoid overextending the
250 interpretations.

251 We further subdivide the mean flow convergence component of the precipitation
252 differences into dynamic and thermodynamic components. Specifically, we decompose the
253 climatological precipitation differences between experiments as

254
$$\delta \bar{P} = -\frac{1}{\rho_w g} \nabla \cdot \int_0^{p_s} ([\delta \bar{\mathbf{u}}] \bar{q} + \bar{\mathbf{u}} [\delta \bar{q}] + \delta \overline{\mathbf{u}' q'}) dp + \delta \bar{E}, \quad (4)$$

255 where the $[\delta \bar{\mathbf{u}}][\delta \bar{q}]$ term has been neglected because it is much smaller than the other terms. The
 256 first term on the right-hand side of (4) represents the impact of the change in climatological
 257 circulation, holding the climatological specific humidity constant. We call this term the circulation
 258 bias term. The second term on the right-hand side of (4), the humidity bias term, captures the
 259 impact of the change in climatological specific humidity, holding the climatological mean flow
 260 constant. These two terms indicate whether the removal of SST biases impacts precipitation more
 261 strongly through changes in specific humidity that accompany SST changes (thermodynamics) or
 262 through impacts of SSTs on the atmospheric circulation, which then impacts precipitation patterns
 263 (dynamics).

264

265 **3. Results**

266 The seasonal North American precipitation biases in the historical FLOR and FLOR-FA
 267 simulations, presented as a percentage relative to the observed climatology, are illustrated in Fig.
 268 5. Consistent with Fig. 1, the reduction of SST biases in FLOR-FA reduces or eliminates the
 269 precipitation biases over portions of western North America. In the extended winter, flux
 270 adjustment reduces precipitation biases over a large portion of North America, although the wet
 271 bias persists in FLOR-FA (Fig. 5c). Observational errors in the precipitation climatology,
 272 however, are clear in the cold season, as a bias discontinuity is apparent at the United States-
 273 Canada border due to differences in precipitation collection technology leading to improved
 274 precision in Canada (Adam and Lettenmaier 2003). In the warm season, the bias reduction is even
 275 stronger, especially over regions most strongly affected by the NAMS and over the Rockies. This

276 finding is consistent with recent work that found superior performance of FLOR-FA in simulating
277 the NAMS (Pascale et al. 2017, 2018). We note, however, that FLOR-FA does exacerbate the dry
278 bias over the south-central U.S. in both seasons. Overall, flux adjustment in FLOR reduces the
279 precipitation climatology root-mean-square error over the U.S. region (25-50°N, 60-130°W) by
280 18.3% in October-March and by 43.4% in April-September. We find nearly identical results when
281 using the other observed precipitation datasets (Figs. S2 and S3).

282

283 *a. TPNP and TANA simulation results*

284

285 Next, we analyze the TPNP and TANA simulation results to attribute in a general sense
286 the importance of Pacific and Atlantic SST biases for the FLOR/FLOR-FA climatological
287 precipitation differences. We begin by analyzing climatological differences in precipitation and
288 atmospheric circulation between the 100-yr CTL and each of the TPNP and TANA simulations
289 (designated as δP_{TPNP} and δP_{TANA} for the TPNP and TANA precipitation differences, respectively).
290 A comparison of these plots with the corresponding CTL minus FA plots reveals the degree to
291 which SST biases in the individual basins can explain the differences in the total SST bias-related
292 precipitation differences over North America.

293 In Fig. 6 we focus on differences in precipitation, sea level pressure (SLP), and 925 hPa
294 wind. The 925 hPa wind corresponds closely with the Caribbean and Great Plains low-level jets,
295 which have a strong impact on the warm season hydroclimate of the central United States (e.g.,
296 Krishnamurthy et al. 2015) and are impacted by coupled model SST biases (e.g., Krishnamurthy
297 et al. 2015, 2019). Consistent with the analysis presented earlier, the CTL simulation produces
298 much wetter conditions over southern North America, especially over the southwestern region,

299 than FA in both the cold and warm seasons (Fig. 6a,b). Figure 6 also reveals that the wetter North
300 America is accompanied by wetter conditions in the equatorial Atlantic and Pacific Oceans, a much
301 deeper wintertime Aleutian low, a weaker summertime North Pacific High and continental low in
302 the North American monsoon region, and a stronger western portion of the summertime North
303 Atlantic Subtropical High (NASH). Fig. 6 presents the precipitation differences as fractional
304 differences relative to the CTL simulation, but the largest absolute differences (shown in Fig. S4)
305 occur in the deep tropics, a region where the differences in convective heating can induce large
306 differences in the extratropical circulation. The cold season composite differences bear a close
307 resemblance to the composites associated with strong El Niño episodes (e.g. Johnson and Kosaka
308 2016), suggesting a role for tropically forced changes in the large-scale circulation and Pacific
309 storm track, which we explore later. Overall, Figs. 6a and b are consistent with large SST-induced
310 differences in atmospheric circulation that result in stronger imports of atmospheric moisture into
311 southern North America in FLOR relative to FLOR-FA.

312 The remainder of Fig. 6 illustrates how much of the CTL/FA differences can be explained
313 by tropical and extratropical North Pacific (Fig. 6c,d) or North Atlantic (Fig. 6e,f) differences.
314 The overall impression is that both TPNP and TANA SST biases, primarily negative (Fig. 2),
315 contribute to drier conditions in northern North America and wetter conditions in southern North
316 America. Surprisingly, the TANA SST differences appear to have a dominant influence on the
317 southern North America precipitation and even the North Pacific atmospheric circulation
318 differences in both seasons. In the cold season, both the TANA and TPNP SST biases induce a
319 strengthened Aleutian low, but the Aleutian low response to TANA SST biases is stronger (Fig.
320 6e). Even more surprisingly, the TANA SST biases induce stronger positive fractional

321 precipitation biases in the equatorial Pacific Ocean than the direct response to Pacific SST biases,
322 at least in the extended winter season.

323 We quantify the impacts of North Atlantic and North Pacific SST biases on the
324 climatological CTL/FA precipitation differences in Fig. 7. Specifically, we calculate the
325 percentage of δP_{FA} that can be attributed to δP_{TPNP} and δP_{TANA} . We mask out regions where the
326 CTL/FA precipitation differences are less than 10% of the CTL climatology to focus on regions
327 where the differences are large. The results of Fig. 7 confirm the visual impression of Fig. 6 in
328 that both Atlantic and Pacific SST biases are important for the continental U.S. during the extended
329 winter, that tropical and/or extratropical North Atlantic (North Pacific) SST biases dominate the
330 impacts over southern (northern) North America, and that the Atlantic SST biases are particularly
331 important over the continental U.S. during the extended summer (Fig. 7d). We note, however, that
332 we should not expect the total impact of North Atlantic and North Pacific SST biases to be a linear
333 superposition of the TPNP and TANA simulation results because the Pacific and Atlantic SST
334 biases affect the SST biases in remote ocean basins, as discussed in Section 3c.

335 The strength of the impact of North Atlantic SST biases on North Pacific precipitation and
336 atmospheric circulation, though surprising, is consistent with recent studies that have examined
337 multi-decadal variability and trends of Atlantic SSTs (Kucharski et al. 2011; McGregor et al. 2014;
338 Li et al. 2016; Ruprich-Robert et al. 2017). In particular, the climate modeling studies of
339 McGregor et al. (2014) and Li et al. (2016) demonstrate that the tropical Atlantic warming trend
340 over the past few decades has the potential to induce negative SST and precipitation trends over
341 the tropical Pacific via modifications of the Walker circulation and coupled ocean/atmosphere
342 feedbacks. These changes in the tropical oceans also impact the circulation and precipitation over
343 the North Pacific and North America (McGregor et al. 2014). Recent studies of Atlantic

344 multidecadal variability reveal consistent results. Anomalously warm conditions in the tropical
345 Atlantic result in negative precipitation anomalies over the tropical Pacific and an anomalously
346 weak Aleutian low, which impacts the downstream North American climate (Sutton and Hodson
347 2007; Kushnir et al. 2010; Ruprich-Robert et al. 2017). The negative tropical Atlantic SST biases
348 in FLOR result in the expected response (opposite to that seen from warming) seen in Fig. 6; that
349 is, a stronger Aleutian low.

350 The results in Fig. 6 generally are consistent with the picture presented above and more
351 generally with the studies of Wang et al. (2007, 2008), which examined the influence of the
352 Atlantic warm pool on Western Hemisphere climate, albeit with a focus only on the summer
353 season. In both the FA and TANA response maps, large negative precipitation differences are
354 present over the tropical Atlantic and northern South America, over and near the regions where
355 tropical Atlantic SST differences are strongly negative. The reduction of atmospheric convection
356 in the Atlantic warm pool results in a “Gill response” (Gill 1980) that manifests as positive SLP
357 differences near and just northwest of the precipitation anomalies (Sutton and Hodson 2007; Wang
358 et al. 2007; Kushnir et al. 2010). The response, however, is not confined to the tropical Atlantic,
359 as the atmospheric Rossby and Kelvin wave response spreads the anomalous cooling to the tropical
360 Pacific, destabilizing the atmosphere and promoting enhanced convection remote from the Atlantic
361 SST forcing (Sutton and Hodson 2007; Kushnir et al. 2010). Therefore, tropical Atlantic cooling
362 promotes a dipole of anomalous convection, with suppressed convection over the tropical western
363 Atlantic and enhanced convection in the central and eastern tropical Pacific.

364 In boreal winter the enhanced tropical Pacific convection resulting from the Atlantic
365 cooling has the potential to force a Pacific/North American-like (PNA-like) circulation pattern that
366 features an enhanced Aleutian low (Sutton and Hodson 2007; Ruprich-Robert et al. 2017), as

367 shown in Fig. 6e. The tropical Pacific SST differences also can induce tropical precipitation
368 differences that induce a strengthened Aleutian low (Fig. 6c), but the response is not as strong,
369 possibly because the tropical Pacific SST differences are not as large as the tropical Atlantic SST
370 differences (Fig. 2) and possibly because the tropical Atlantic atmospheric convection anomalies
371 are well positioned to induce remote coupled ocean-atmosphere feedbacks in the tropical Pacific
372 basin (Li et al. 2016; Ruprich-Robert et al. 2017). We examine the remote SST impacts of the
373 Atlantic SST biases in Section 3c.

374 In the summer months, the Atlantic SST differences potentially can exert stronger direct
375 impacts on North American precipitation (Wang et al. 2007, 2008; Kushnir et al. 2010). Figure 6f
376 indicates positive SLP differences between CTL and TANA over the western tropical Atlantic and
377 over southern North America, which indicate a strengthened western portion of the NASH and a
378 weakened North American monsoon low. This pattern is consistent with the climate model
379 experiments of Wang et al. (2007, 2008) that demonstrated the role of the Atlantic warm pool in
380 modifying the strength of the summertime NASH and the Great Plains and Caribbean low-level
381 jets, which then impacts the northward moisture transport and precipitation in the central U.S.
382 (Wang et al. 2008).

383 Overall, the results presented in this section suggest both Pacific and Atlantic SST biases
384 prominently drive North American precipitation biases. We also suggest plausible mechanisms
385 that are consistent with previous studies that focused primarily on the impacts of Pacific and
386 Atlantic SST variability. We next examine the roles of tropical and extratropical SST biases, the
387 inter-basin links among the SST biases, and precipitation budget diagnostics to determine if the
388 arguments presented above hold up to further scrutiny.

389

390 *b. TP and TA simulation results*

391

392 The arguments regarding the prominent role of Atlantic SST biases on the North Pacific
393 circulation and North American precipitation suggest that tropical rather than extratropical Atlantic
394 SST biases play the more crucial role. The reason is that tropical Atlantic SST biases can directly
395 influence moisture advection into the US, and tropical SST biases can more easily induce upstream
396 circulation impacts due to the larger length scales of the atmospheric response in the tropics
397 relative to the extratropics. To investigate this hypothesis, we show the CTL/TP and CTL/TA
398 seasonal composite differences in circulation and precipitation in Fig. 8. Consistent with
399 expectations, the tropical Atlantic SST biases appear to dominate the Atlantic SST effects on
400 circulation and North American precipitation. In both seasons, the TA results are similar to those
401 of TANA (compare Fig. 8c,d with Fig. 6e,f). The tropical Atlantic precipitation and hemispheric
402 circulation response in the TA results are slightly stronger than that of the TANA experiment,
403 indicating that the extratropical Atlantic SST biases act to damp the full Atlantic SST response
404 slightly, particularly in the extended summer. The reason for this damping requires further
405 investigation, but it appears that colder North Atlantic sea surface in FLOR can induce a stronger
406 NASH that increases moisture convergence in the Caribbean Sea, partially offsetting the reduced
407 moisture and atmospheric instability owing to the colder tropical Atlantic sea surface. The
408 offsetting influence of the extratropical North Atlantic SSTs is consistent with the GCM
409 experiments of Okumura et al. (2009), who investigated the mechanisms by which a large
410 freshwater forcing of the North Atlantic can impact North Pacific climate.

411 Examination of the TP results suggests that for the Pacific, both tropical and extratropical
412 SST biases contribute to North American precipitation biases in the boreal cold season (compare

413 Fig. 6c with Fig. 8a) but that tropical SST biases play little role in the boreal warm season. The
414 enhanced subtropical convection in CTL relative to TP in the cold season (Fig. 8a) where CTL
415 SST biases are positive (Fig. 2) may contribute to the slightly stronger Aleutian low through a
416 poleward propagating Rossby wave response. The tropical Pacific SST biases, however, are small
417 relative to the extratropical biases (Fig. 2). The strongly negative SST biases in the central North
418 Pacific in CTL increase the baroclinicity, which also enhances the North Pacific storm track into
419 southern North America. We examine storm track changes more closely in Section 3d. Overall,
420 we find that in the dynamically active boreal cold season, both tropical and extratropical North
421 Pacific SST biases have a substantial impact on FLOR's simulation of North American
422 precipitation. This contrasts the interannual variability of North American precipitation, in which
423 tropical Pacific SSTs are believed to play a much stronger role than extratropical Pacific SST
424 variability (e.g. Kushnir et al. 2002). A key difference is that FLOR's pattern of mean SST biases
425 (with strong biases in the extratropics and in the tropical Atlantic), looks quite different from
426 ENSO SST anomalies, which typically have their strongest signature in the central and eastern
427 equatorial Pacific.

428

429 *c. TPNP_{iso} and TANA_{iso} simulation results*

430

431 As discussed above, the SST biases in the North Atlantic and the North Pacific can induce
432 nonlocal SST biases through atmospheric and oceanic pathways. Therefore, the TANA and TPNP
433 simulations do not necessarily isolate the impacts of the SST biases in the basins for which the
434 SSTs have been restored. We illustrate the non-local SST impacts in Fig. 9, which shows the
435 differences in annual mean climatological SSTs between the CTL and each of the TPNP and

436 TANA simulations. By construction, the SST differences over the North Pacific (North Atlantic)
437 domains defined in Fig. 3 for the TPNP (TANA) simulation are nearly equal to the CTL/FA
438 differences. The SST differences in all other ocean basins are remotely forced.

439 The SST differences between the CTL and TANA simulation (Fig. 9) reveal that the
440 negative tropical and North Atlantic SST biases induce strongly negative SST biases in the
441 extratropical North Pacific, strongest near 40°N. The North Pacific response to Atlantic SST
442 forcing is consistent with past North Atlantic “water hosing” experiments (Zhang and Delworth
443 2005; Okumura et al. 2009) in which the North Atlantic is cooled through a large freshwater input
444 as well as recent studies on Atlantic multidecadal variability (Zhang and Delworth 2007; Ruprich-
445 Robert et al. 2017; Johnson et al. 2018) and climate model SST biases (Wang et al. 2014; Zhang
446 and Zhao 2014). Wang et al. (2014) demonstrate that the strength of AMOC may be a key factor
447 in the link between North Pacific and North Atlantic SST biases in the models participating in
448 CMIP5.

449 Similarly, the tropical and North Pacific SST biases remotely force Atlantic SST biases
450 (Fig. 9a), although the overall impact is not as strong as that of the Atlantic on the Pacific. The
451 negative SST differences over much of the North Atlantic indicate that the removal of the North
452 Pacific SST biases in the TPNP simulation also reduces the negative SST biases in portions of the
453 North Atlantic. In the sub-Arctic North Atlantic, the SST differences are positive, possibly
454 reflecting a shift of the Gulf Stream or changes in the AMOC and oceanic deep convection.
455 Although the amplitude of remote Atlantic SST changes (Fig. 9a) is considerably less than that of
456 the remote Pacific SST changes (Fig. 9b), the North Pacific SST biases induce substantial
457 decreases in the North Atlantic meridional SST gradient (Fig. 9a) and baroclinicity in vicinity of

458 the North Atlantic storm track, which, as shown in the following section, result in notable increases
459 in evaporation (Figs. 12 and 13) and a reduced storm track intensity (Fig. 15).

460 To distinguish the roles of local versus remotely forced SST biases, we examine the results
461 of the TANA_{iso} and TPNP_{iso} experiments following the decompositions given in (1) and (2). The
462 decomposition of the Atlantic SST bias effect given by (2) is illustrated in Fig. 10. The top panels
463 show notably stronger precipitation differences over North America than the bottom panels, which
464 indicate a dominance of the locally forced Atlantic SST bias effects. In October – March, the
465 remotely forced effects (Fig. 10c) are consistent with those of the TPNP experiments, indicating
466 that the North Pacific cooling induced by the negative tropical and North Atlantic SST biases
467 induces drying over northern North America and wetting over southern North America. The local
468 and nonlocal Atlantic SST bias effects oppose each other in northern North America but reinforce
469 each other over southern North America (compare Figs. 10a with 10c). In April – September, the
470 local and nonlocal effects oppose each other over most of North America, but the local Atlantic
471 SST effects dominate even more than in the boreal cold season.

472 The decomposition of the Pacific SST bias effect reveals a more complicated picture (Fig.
473 11), particularly in the boreal cold season. In October – March over southwestern North America,
474 the local and remote TPNP SST effects reinforce each other, indicating that the negative SST
475 biases in both ocean basins result in increased precipitation. In other parts of North America, the
476 two effects tend to oppose each other. Most conspicuously, the negative TPNP SST bias pattern
477 directly results in positive SLP differences over the North Pacific (Fig. 11a), but the negative SST
478 differences induced in the tropical and North Atlantic (Fig. 9a) force negative SLP differences
479 over the North Pacific (Fig. 11c) that overcompensate the positive SLP differences. This

480 cancellation between the direct and indirect effect over the North Pacific explains why the impact
481 of the North Pacific SST biases on the North Pacific circulation is relatively modest (Fig. 6c).

482 The positive SLP response to the negative SST differences over the North Pacific (Fig.
483 11a) resembles the direct, linear baroclinic response to extratropical SSTs noted in previous studies
484 (Peng et al. 1997; Peng and Whitaker 1999; Kushnir et al. 2002). Specifically, the North Pacific
485 high diminishes in amplitude with height (not shown), consistent with the expected direct response
486 to shallow cooling. However, the total response to extratropical cooling is strongly mediated by
487 synoptic eddies, which is highly sensitive to the background flow (Peng et al. 1997). The total
488 eddy-mediated response to North Pacific cooling in Fig. 11a, with a surface high over the North
489 Pacific and an upper-level trough extending from the eastern Pacific over much of North America
490 (not shown) resembles the response to North Pacific SST anomalies with February background
491 conditions studied in Peng et al. (1997) and Peng and Whitaker (1999). However, those previous
492 studies showed that the response pattern is quite distinct with January background conditions,
493 demonstrating that the synoptic eddy-mediated response to North Pacific extratropical SST
494 anomalies is highly sensitive to the background climatology. Therefore, we urge caution to avoid
495 over generalizing these results.

496 The remote Pacific SST bias effect over North America is substantial in October – March
497 (Figs. 11c) and generally consistent with the local Atlantic SST bias effect (Fig. 10a). In the
498 context of all other simulation results and previous studies noted above, this finding reinforces that
499 negative tropical Atlantic SST biases in the boreal cold season are effective in inducing an
500 anomalously deep Aleutian low and anomalously wet conditions over much of southern North
501 America. Moreover, a substantial portion of the negative tropical Atlantic SST biases are remotely

502 forced by the North Pacific SST biases. In the boreal warm season, however, the remotely forced
503 effect of North Pacific SST biases over North America is small (Fig. 11d).

504

505 *d. Precipitation budget diagnostics*

506

507 To gain additional insight into the mechanisms that connect SST biases to North American
508 precipitation biases, we examine the contributions to the simulations' climatological precipitation
509 differences determined from equation (4). Specifically, we focus on the circulation bias, humidity
510 bias, and evaporation terms, as these terms generally are the largest contributors to the
511 climatological precipitation differences. As we note above we cannot derive accurate estimates of
512 the contributions by transient eddy convergence owing to insufficient diagnostic output. To shed
513 light on the possible role of differences in transient eddies, we examine differences in the
514 climatological storm tracks.

515 We first focus on the climatological differences in October – March (Fig. 12). Overall, the
516 circulation bias and evaporation terms make the greatest contributions to the precipitation
517 differences over the North American continent for each pair of experiments. In general, the
518 humidity bias term tends to oppose the changes from the circulation bias term, but the effects of
519 the changing circulation dominate over the thermodynamic effects. Both the TPNP (Fig. 12b) and
520 TANA (Fig. 12c) experiments capture the CTL minus FA circulation bias pattern, with the TANA
521 differences generally showing stronger magnitudes. These findings indicate that the climatological
522 circulation changes induced by the North Pacific and especially tropical Atlantic SST biases
523 dominate the SST-induced differences in wintertime climatological precipitation over North
524 America.

525 However, there are a number of regions where the circulation bias effects are not the
526 dominant factor during the extended winter season. The CTL minus FA circulation bias pattern
527 (Fig. 12a) features negative differences over Baja California, parts of western North America, and
528 a portion of the southwestern U.S., which contrast the positive precipitation biases in FLOR over
529 this region. These negative circulation-induced differences are overwhelmed by the effects of
530 evaporation (Fig. 12g) and, to a lesser extent, the humidity bias term (Fig. 12d). These opposing
531 influences are captured well in the TPNP experiment (Fig. 12b,e,h). The residual term (bottom
532 row of Fig. 12) generally features positive differences in southern North America and negative
533 differences over the northwest coast of North America. This residual likely reflects, in large part,
534 the omission of the change in transient eddy fluxes from the change in storm tracks, as discussed
535 below.

536 In contrast with the extended winter, all three terms make sizeable contributions to the
537 climatological precipitation differences from April – September (Fig. 13). Once again, the
538 humidity bias term (second row) tends to oppose the effects of the corresponding circulation term
539 (top row). The combination of the three terms results in a tendency for positive precipitation biases
540 over most of North America (Fig. 4d), but the dominant term varies regionally. Overall, the TANA
541 experiment (right column) captures the total difference patterns (left column) rather well for all
542 three terms, confirming the dominance of the Atlantic SST biases on the SST-related
543 climatological precipitation biases over North America in the FLOR model.

544 Changes in the storm tracks also modify the transient eddy moisture flux convergence,
545 thereby also contributing to the climatological precipitation differences. Figure 14 provides the
546 climatological storm tracks in CTL, FA, and in reanalysis data for both the extended winter and
547 summer. Compared with CTL (Fig. 14c,f), FA features more northerly displaced North Pacific

548 and North Atlantic storm tracks in both seasons (Fig. 14b,e), with a somewhat weaker storm track
549 in the western North Pacific in boreal winter. The northward shift of the storm tracks in FA results
550 in improved agreement with the position of the storm tracks derived from reanalysis data (Fig.
551 14a,b), although the stronger storm track in CTL more closely matches reanalysis data in the
552 western North Pacific region. Overall, Fig. 14 indicates that the SST biases in CTL result in a
553 southward bias in the location of the dominant Northern Hemisphere storm tracks.

554 The differences in the storm tracks between CTL and FA (Fig. 15a,b) clearly show the
555 southerly displacement over both basins and the stronger North Pacific storm track in CTL. The
556 winter difference pattern resembles, in many respects, the storm track response to El Niño (e.g.,
557 Johnson and Kosaka 2016) as well as to the negative phase of the Atlantic Multidecadal Oscillation
558 (Zhang and Delworth 2007), which suggests that SST biases in both the Pacific and Atlantic may
559 contribute to these differences. Consistently, both the TPNP (Fig. 15c,d) and TANA experiments
560 (Fig. 15e,f) produce similar changes to the storm tracks, indicating that both the Atlantic and
561 Pacific SST biases contribute to the stronger and southerly displaced storm tracks in CTL. The
562 storm track differences shown in Fig. 15 closely mirror the differences in 200 hPa zonal wind. The
563 southerly bias in the North Pacific storm track in CTL likely contributes to the wetter conditions
564 in southwestern and drier conditions in northwestern North America relative to FA, a conclusion
565 that is corroborated by the estimated transient eddy contributions to the precipitation budgets,
566 although we choose not to show these results because the insufficient spatial diagnostic outputs
567 limit the reliability of these estimates (Section 2c).

568

569 **4. Discussion and Conclusions**

570

571 In this study, we have examined the role of SST biases on the simulation of North American
572 climatological precipitation in a global climate model with 50 km atmospheric horizontal
573 resolution, the GFDL FLOR model. Like many climate models, FLOR simulates excessive
574 precipitation over much of western North America, leading to a failure to simulate the strong east-
575 west contrast in climatological precipitation in observations. A flux-adjusted version of FLOR
576 that greatly reduces SST biases mitigates this deficiency in continental precipitation, indicating
577 that SST biases are a contributor to these precipitation biases. Previous investigations have
578 reached similar conclusions regarding the simulation of the NAMS (Liang et al. 2008; Pascale et
579 al. 2017, 2018), the Great Plains and Caribbean Low-Level Jets (Krishnamurthy et al. 2019), Gulf
580 of California moisture surges into southwestern North America (Pascale et al. 2016), and western
581 United States climatological precipitation in general (Mejia et al. 2018), but the present study
582 focuses on the pathways by which Atlantic and Pacific SST biases contribute to the simulation of
583 excessive precipitation. The main findings of the study are summarized in schematic diagrams
584 shown in Fig. 16. Because the SST biases in FLOR share many features common to many or even
585 most current global climate models (e.g., Wang et al. 2014; Richter 2015), the results presented
586 here likely apply broadly to a range of climate models.

587 From the analysis presented here, a few general themes emerge. First, relative to the
588 Pacific, FLOR’s Atlantic SST biases make a substantially greater contribution to the excessive
589 precipitation in the western U.S. and Mexico for both seasons. One reason appears to be
590 substantially stronger SST biases in the tropical Atlantic relative to the tropical Pacific in FLOR,
591 given that tropical SST biases are most effective in exciting large-scale circulation responses
592 owing to their effects on tropical convection and Rossby wave sources. Although the relative
593 strength of the tropical Pacific SST biases may differ in other climate models, the strong tropical

594 Atlantic SST biases are pervasive in the current generation of global climate models (Li and Xie
595 2014; Wang et al. 2014). Another factor is the effectiveness of tropical Atlantic SST biases to
596 induce substantial circulation and moisture anomalies both locally, through changes in the NASH
597 and associated low-level jets, and nonlocally in the Indian and Pacific Oceans, through
598 modifications of the Walker circulation. The latter mechanism, which has been corroborated in
599 several recent studies on Atlantic multidecadal variability, results in a strong link between negative
600 SST biases in the tropical Atlantic and an anomalously deepened Aleutian low and an associated
601 southerly shift of the storm tracks, which contribute substantially to the wet bias over western
602 North America. Overall, these findings suggest that reductions of tropical Atlantic SST biases in
603 coupled GCMs, which appear to be closely tied to biases in the Atlantic meridional overturning
604 circulation (Wang et al. 2014), would have substantial benefits for the simulation of precipitation
605 over the United States and Central America, especially in boreal summer.

606 Another emerging theme is the difficulty in isolating the effects of local SST biases owing
607 to precipitation responses to remote SST effects, e.g., the response of precipitation to the SST
608 changes induced in the North Pacific by Atlantic SST biases. Negative SST biases in the Atlantic
609 induce negative SST biases in the extratropical Pacific, and negative SST biases in the North
610 Pacific induce negative SST biases in both the tropical and extratropical North Atlantic. Both the
611 local and remotely forced SST biases appear to have substantial influences on the atmospheric
612 circulation and North American precipitation. Another apparently important factor for the reduced
613 impact of the North Pacific SST biases relative to North Atlantic SST biases is the competing
614 impacts of the local North Pacific and remotely forced SST bias impacts on the North Pacific
615 atmospheric circulation. Specifically, the North Pacific surface high forced by local negative SST
616 biases partially offsets the deepened Aleutian low response to the remotely forced negative tropical

617 Atlantic SST biases (Fig. 11a,c). However, these competing effects may be challenging to
618 disentangle in studies with multi-model ensembles, as previous studies have demonstrated that the
619 eddy-mediated response to extratropical SST forcing is sensitive to the details of the background
620 flow.

621 As discussed in Section 1, various processes and modeling deficiencies contribute to the
622 pervasive SST biases in the current generation of global climate models. As both
623 parameterizations improve and model resolution increases, we expect that these SST biases
624 accordingly shall reduce. The findings presented here provide insight into the expected changes
625 in climatological precipitation over North America as these SST biases are reduced, regardless of
626 whether the precipitation biases in other models are stronger or weaker than those of FLOR. This
627 study also suggests that flux adjustment may remain a viable intermediate solution for problems
628 for which climatological precipitation simulation is critical. For example, the improved simulation
629 of the North American monsoon in FLOR-FA has enabled new insights into projected changes of
630 this monsoon system under global warming (Pascale et al. 2017, 2018). These recent studies
631 illuminate how the climate sensitivity of some facets of the climate system may be affected by
632 climatological SST biases and how the removal of these biases through flux adjustment can
633 improve confidence in projected changes. In addition, a set of seasonal hindcasts with FLOR-FA
634 successfully captured the western U.S. precipitation pattern during the El Niño winter of 2015-16,
635 a pattern that was generally poorly predicted and atypical of other strong El Niño events (Yang et
636 al. 2018). This finding raises questions about how the reduction of SST biases may impact seasonal
637 forecasts of western U.S. precipitation. Future work shall address how SST biases may impact
638 other aspects of the variability, prediction skill, and projected changes of North American
639 precipitation, including the tails of precipitation distribution.

640

641 *Acknowledgments.*

642 We thank three anonymous reviewers for constructive comments that greatly benefited this
643 manuscript. We also thank Drs. Liping Zhang and Xiaosong Yang for helpful comments on an
644 earlier version of the manuscript. N. C. Johnson, L. Krishnamurthy, and S. Pascale were supported
645 by awards NA14OAR4320106 and NA18OAR4320123 from the National Oceanic and
646 Atmospheric Administration, U.S. Department of Commerce. NCEP/NCAR Reanalysis and
647 precipitation data are provided by the NOAA/OAR/ESRL PSD, Boulder, Colorado, USA, from
648 their Web site at <http://www.esrl.noaa.gov/psd/>.

649

650

651

References

652 Adam, J.C. and D. P. Lettenmaier, 2003: Adjustment of global gridded precipitation for systematic
653 bias. *JGR:Atmospheres*, 108(D9), doi:[10.1029/2002JD002499](https://doi.org/10.1029/2002JD002499).

654

655 Adcroft, A. J., and Co-authors, 2019: The GFDL global ocean and sea ice model OM4.0: Model
656 description and simulation features. *J. Adv. Model. Earth Syst.*, doi:10.1029/2019MS001726.

657

658 Balaji, V., I. Held, M. Winton, S. Malyshev, and R. Stouffer, 2006: The Exchange Grid: A
659 mechanism for data exchange between Earth System components on independent grids. *Parallel*
660 *Computational Fluid Dynamics: Theory and Applications: Proceedings of the 2005 International*
661 *Conference on Parallel Computational Fluid Dynamics*, A. Deane et al., Eds., Elsevier, 33–41.

662

663 Chen, M., P. Xie, J. E. Janowiak, and P. A. Arkin, 2002: Global Land Precipitation: A 50-yr
664 Monthly Analysis Based on Gauge Observations, *J. Hydrometeorology*, **3**, 249-266.
665

666 Dai, A., 2006: Precipitation characteristics in eighteen coupled climate models. *J. Climate*, **19**,
667 4605-4630.
668

669 Dai, A., and K. E. Trenberth, 2004: The diurnal cycle and its depiction in the Community Climate
670 System Model. *J. Climate*, **17**, 930-951.
671

672 Delworth, T. L., and Coauthors, 2012: Simulated climate and climate change in the GFDL CM2.5
673 high-resolution coupled climate model. *J. Climate*, **25**, 2755-2781, doi:10.1175/JCLI-D-11-
674 00316.1.
675

676 Geil, K. L., Y. L. Serra, and X. Zeng, 2013: Assessment of CMIP5 Model Simulations of the North
677 American Monsoon System. *J. Climate*, **26**, 8787-8801.
678

679 Gill, A. E., 1980: Some simple solutions for heat-induced tropical circulation. *Quart. J. Roy.*
680 *Meteor. Soc.*, **106**, 447-462.
681

682 Griffies, S. M., and Co-authors, 2015: Impacts on ocean heat from transient mesoscale eddies in a
683 hierarchy of climate models. *J. Climate*, **28**, 952-977, doi: 10.1175/JCLI-D-14-00353.1.
684

685 Held, I. M., and Co-authors, 2019: Structure and performance of GFDL's CM4.0 climate model.
686 *J. Adv. Model. Earth Syst.*, in press, doi:10.1029/2019MS001829.
687

688 Jia, L., and Co-authors, 2015: Improved seasonal prediction of temperature and precipitation over
689 land in a high-resolution GFDL climate model. *J. Climate*, **28**, 2044-2062, doi:10.1175/JCLI-D-
690 14-00112.1.
691

692 Jia, L., G. A. Vecchi, X. Yang, R. G. Gudgel, T. L. Delworth, W. F. Stern, K. Paffendorf, S. D.
693 Underwood, and F. Zeng, 2016: The roles of radiative forcing, sea surface temperatures, and
694 atmospheric and land initial conditions in U.S. summer warming episodes. *J. Climate*, **29**, 4121-
695 4135, doi:10.1175/JCLI-D-15-0471.1.
696

697 Jiang, X., B. Xiang, M. Zhao, T. Li, S.-J. Lin, Z. Wang, and J.-H. Chen, 2018: Intraseasonal
698 Tropical Cyclogenesis Prediction in a Global Coupled Model System. *J. Climate*, **31**, 6209-6227,
699 doi:[10.1175/JCLI-D-17-0454.1](https://doi.org/10.1175/JCLI-D-17-0454.1).
700

701 Johnson, N. C., and Y. Kosaka, 2016: The impact of eastern equatorial Pacific convection on the
702 diversity of boreal winter El Niño teleconnection patterns. *Climate Dyn.*, **47**, 3737-3764,
703 doi:10.1007/s00382-016-3039-1.
704

705 Johnson, N. C., S.-P. Xie, Y. Kosaka, and X. Li, 2018: Increasing occurrence of cold and warm
706 extremes during the recent global warming slowdown. *Nature Communications*, **9**, 1724,
707 doi:10.1038/s41467-018-04040-y.

708

709 Kalnay E., and Co-authors, 1996: The NCEP/NCAR 40-Year Reanalysis Project. *Bull. Amer.*
710 *Meteor. Soc.*, **77**, 437-471.

711

712 Kapnick, S. B. X. Yang, G. A. Vecchi, T. L. Delworth, R. Gudgel, S. Malyshev, P. C. D. Milly,
713 E. Shevliakova, S. Underwood, and S. A. Margulis, 2018: Potential for western US seasonal
714 snowpack prediction. *Proc. Nat. Acad. Sci.*, **115**, 1180-1185, doi:10.1073/pnas.1716760115.

715

716 Keeley, S. P. E., R. T. Sutton, and L. C. Shaffrey, 2012: The impact of North Atlantic sea surface
717 temperature errors on the simulation of North Atlantic European region climate. *Q. J. Roy. Met.*
718 *Soc.*, **138**, 1774-1783.

719

720 Kirtman, B. P., and Co-authors, 2012: Impact of ocean model resolution on CCSM climate
721 simulations. *Clim. Dyn.*, **39**, 1303-1328, doi:10.1007/s00382-012-1500-3.

722

723 Krishnamurthy, L., A. G. Muñoz, G. A. Vecchi, R. Msadek, A. T. Wittenberg, B. Stern, R. Gudgel,
724 and F. Zeng, 2019: Assessment of summer rainfall forecast skill in the Intra-Americas in GFDL
725 high and low-resolution models. *Climate Dyn.*, **52**, 1965-1982, doi: 10.1007/s00382-018-4234-z.

726

727 Krishnamurthy, L., G. A. Vecchi, R. Msadek, A. Wittenberg, T. L. Delworth, and F. Zeng, 2015:
728 The seasonality of the Great Plains low-level jet and ENSO relationship. *J. Climate*, **28**, 4525-
729 4544, doi:10.1175/JCLI-D-14-00590.1.

730

731 Kucharski, F., I.-S. Kang, R. Farneti, and L. Feudale, 2011: Tropical Pacific response to 20th
732 century Atlantic warming. *Geophys. Res. Lett.*, **38**, L03702, doi:10.1029/2010GL046248.
733

734 Kushnir, Y., W. A. Robinson, I. Bladé, N. M. J. Hall, S. Peng, R. Sutton, 2002: Atmospheric GCM
735 response to extratropical SST anomalies: Synthesis and evaluation. *J. Climate*, **15**, 2233-2256.
736

737 Kushnir, Y., R. Seager, M. Ting, N. Naik, and J. Nakamura, 2010: Mechanisms of tropical Atlantic
738 SST influence on North American precipitation variability. *J. Climate*, **23**, 5610-5628,
739 doi:10.1175/2010JCLI3172.1.
740

741 Large, W. G., and G. Danabasoglu, 2006: Attribution and impacts of upper-ocean biases in
742 CCSM3. *J. Climate*, **19**, 2325-2346.
743

744 Li, G., and S.-P. Xie, 2014: Tropical biases in CMIP5 multimodel ensemble: The excessive
745 equatorial Pacific cold tongue and double ITCZ problems. *J. Climate*, **27**, 1765-1780.
746

747 Li, X., S.-P. Xie, S. T. Gille, and C. Yoo, 2016: Atlantic-induced pan-tropical climate change over
748 the past three decades. *Nature Clim. Change*, **6**, 275-279, doi:10.1038/nclimate2840.
749

750 Liang, X.-Z., J. Zhu, K. E. Kunkel, M. Ting, and J. X. L. Wang, 2008: Do CGCMs simulate the
751 North American monsoon precipitation seasonal-interannual variability? *J. Climate*, **21**, 4424-
752 4448.
753

754 Lin, J.-L., 2007: The double-ITCZ problem in IPCC AR4 coupled GFCMs: Ocean-atmosphere
755 feedback analysis. *J. Climate*, **20**, 4497-4525.
756

757 Liu, Z., A. Mehran, T. J. Phillips, and A. AghaKouchak, 2014: Seasonal and regional biases in
758 CMIP5 precipitation simulations. *Clim. Res.*, **60**, 35-40, doi: 10.3354/cr01221.
759

760 McGregor, S., A. Timmermann, M. F. Stuecker, M. H. England, M. Merrifield, F.-F. Jin, and Y.
761 Chikamoto, 2014: Recent Walker circulation strengthening and Pacific cooling amplified by
762 Atlantic warming. *Nature. Clim. Change*, **4**, 888-892, doi:10.1038/nclimate2330.
763

764 Mechoso, C., and Coauthors, 1995: The seasonal cycle over the tropical Pacific in coupled ocean-
765 atmosphere general circulation models. *Mon Wea. Rev.*, **123**, 2825-2838.
766

767 Mehran, A., A. AghaKouchak, and T. J. Phillips, 2014: Evaluation of CMIP5 continental
768 precipitation simulations relative to satellite-based gauge-adjusted observations. *J. Geophys. Res.*,
769 **119**, 1695-1707, doi:10.1002/2013JD021152.
770

771 Mejia, J. F., D. Koračin, and E. M. Wilcox, 2018: Effect of coupled global climate models sea
772 surface temperature biases on simulated climate of the western United States. *Int. J. Climatol.*, **38**,
773 5386-5404, doi:10.1002/joc.5817.
774

775 Murakami, H., G. Villarini, G. A. Vecchi, W. Zhang, and R. Gudgel, 2016: Statistical-dynamical
776 seasonal forecast of North Atlantic and U.S. landfalling tropical cyclones using the high-resolution
777 GFDL FLOR coupled model. *Mon. Wea. Rev.* **144**, 2101-2123, doi:10.1175/MWR-D-15-0308.1.

778

779 Okumura, Y. M., C. Deser, A. Hu, A. Timmermann, and S.-P. Xie, 2009: North Pacific climate
780 response to freshwater forcing in the subarctic North Atlantic: Oceanic and atmospheric pathways.
781 *J. Climate*, **22**, 1424-1445, doi:10.1175/2008JCLI2511.1.

782

783 Pascale, S., W. R. Boos, S. Bordoni, T. L. Delworth, S. B. Kapnick, H. Murakami, G. A. Vecchi,
784 and W. Zhang, 2017: Weakening of the North American monsoon with global warming. *Nature*
785 *Clim. Change*, **7**, 806-812, doi:10.1038/nclimate3412.

786

787 Pascale, S., S. Bordoni, S. B. Kapnick, G. A. Vecchi, T. L. Delworth, S. Underwood, and W.
788 Anderson, 2016: The impact of horizontal resolution on North American monsoon Gulf of
789 California moisture surges in a suite of coupled global climate models. *J. Climate*, **29**, 7911-7936.

790

791 Pascale, S., S. B. Kapnick, S. Bordoni, and T. L. Delworth, 2018: The influence of CO2 forcing
792 on North American Monsoon moisture surges. *J. Climate*, **31**, 7949-7968.

793

794 Pascale, S., V. Lucarini, X. Feng, A. Porporato, and S. ul Hasson, 2015: Analysis of rainfall
795 seasonality from observations and climate models. *Climate Dyn.*, **44**, 3281-3301,
796 doi:10.1007/s00382-014-2278-2.

797

798 Peng, S., W. A. Robinson, and M. P. Hoerling, 1997: The modeled atmospheric response to
799 midlatitude SST anomalies and its dependence on background circulation states. *J. Climate*, **10**,
800 971-987.

801

802 Peng, S. and J. S. Whitaker, 1999: Mechanisms determining the atmospheric response to
803 midlatitude SST anomalies. *J. Climate*, **12**, 1393-1408.

804

805 Phillips, T. J. and P. J. Gleckler, 2006: Evaluation of continental precipitation in 20th century
806 climate simulations: The utility of multimodel statistics. *Water Resources Res.*, **42**, W03202,
807 doi:10.1029/2005WR004313.

808

809 Rayner, N. A., D. E. Parker, E. B. Horton, C. K. Folland, L. V. Alexander, D. P. Rowell, E. C.
810 Kent, and A. Kaplan, 2003: Global analyses of sea surface temperature, sea ice, and night marine
811 air temperature since the late nineteenth century. *J. Geophys. Res.*, **108**, 4407,
812 doi:10.1029/2002JD002670.

813

814 Richter, I., 2015: Climate model biases in the eastern tropical oceans: causes, impacts, and ways
815 forward. *WIREs Clim. Change*, **6**, 345-358.

816

817 Ruprich-Robert, Y., R. Msadek, F. Castruccio, T. Delworth, and G. Danabasoglu, 2017: Assessing
818 the climate impacts of the observed Atlantic Multidecadal Variability using GFDL CM2.1 and
819 NCAR CESM1 global coupled models. *J. Climate*, in press, doi:10.1175/JCLI-D-16-0127.1

820

821 Schneider, U., A. Becker, P. Finger, A. Meyer-Christoffer, M. Ziese, and B. Rudolf, 2014: GPCC's
822 new land surface precipitation climatology based on quality-controlled in situ data and its role in
823 quantifying the global water cycle. *Theor. Appl. Climatol.*, **115**, 15–40,
824 doi:<https://doi.org/10.1007/s00704-013-0860-x>.

825

826 Seager, R., and N. Henderson, 2013: Diagnostic computation of moisture budgets in the ERA-
827 Interim Reanalysis with reference to analysis of CMIP-archived atmospheric model data. *J.*
828 *Climate*, **26**, 7876-7901, doi:10.1175/JCLI-D-13-00018.1.

829

830 Stephens, G. L., T. L'Ecuyer, R. Forbes, A. Gettleman, J.-C. Golaz, A. Bodas-Salcedo, K. Suzuki,
831 P. Gabriel, and J. Haynes, 2010: Dreary state of precipitation in global models. *J. Geophys. Res.*,
832 **115**, D24211, doi:10.1029/2010JD014532.

833

834 Sheffield J., and Co-authors, 2013: North American climate in CMIP5 experiments. Part I:
835 Evaluation of historical simulations of continental and regional climatology. *J. Climate*, **26**, 9209-
836 9245.

837

838 Sutton, R. T., and D. L. R. Hodson, 2007: Climate response to basin-scale warming and cooling
839 of the North Atlantic Ocean. *J. Climate*, **20**, 891-907.

840

841 Sun, Y., S. Solomon, A. Dai, and R. W. Portmann, 2006: How often does it rain? *J. Climate*, **19**,
842 916-934.

843

844 Trenberth, K. E., A. Dai, R. M. Rasmussen, and D. B. Parsons, 2003: The changing character of
845 precipitation. *Bull. Amer. Meteor. Soc.*, **84**, 1205-1217.

846

847 Van der Wiel, K., S. B. Kapnick, G. A. Vecchi, W. F. Cooke, T. L. Delworth, L. Jia, H. Murakami,
848 S. Underwood, and F. Zeng. (2016): "The Resolution Dependence of Contiguous U.S.
849 Precipitation Extremes in Response to CO₂forcing." *Journal of Climate* 29 (22): 7991-8012.
850 doi:10.1175/JCLI-D-16-0307.1

851

852 Vecchi, G. A., and Co-authors., 2014: On the seasonal forecasting of regional tropical cyclone
853 activity. *J. Climate*, **27**, 7994-8016.

854

855 Vecchi, G. A., and Co-authors, 2019: Tropical cyclone sensitivities to CO₂ doubling: Roles of
856 atmospheric resolution, synoptic variability and background climate changes. *Climate Dyn.*, **53**,
857 5999-6033, doi:10.1007/s00382-019-04913-y.

858

859 Wang, C., S.-K. Lee, and D. B. Enfield, 2007: Impact of the Atlantic warm pool on summer climate
860 of the Western Hemisphere. *J. Climate*, **20**, 5021-5040, doi:10.1175/JCLI4304.1.

861

862 Wang, C., S.-K. Lee, and D. B. Enfield, 2008: Climate response to anomalously large and small
863 Atlantic warm pools during the summer. *J. Climate*, **21**, 2437-2450, doi:10.1175/JCLI2029.1.

864

865 Wang, C., L. Zhang, S.-K. Lee, L. Wu, and C. R. Mechoso, 2014: A global perspective on CMIP5
866 climate model biases. *Nature. Clim. Change*, **4**, 201-205.

867
868 Wilcox, E. M. and L. J. Donner, 2007: The frequency of extreme rain events in satellite rain-rate
869 estimates and an atmospheric General Circulation Model. *J. Climate*, **20**, 53-69.

870
871 Willmott, C. J., and K. Matsuura, 2001: Terrestrial air temperature and precipitation: Monthly and
872 annual time series (1950 - 1999),
873 http://climate.geog.udel.edu/~climate/html_pages/README.ghcn_ts2.html.

874
875 Wittenberg, A. T., G. A. Vecchi, T. L. Delworth, A. Rosati, W. Anderson, W. F. Cooke, S.
876 Underwood, F. Zeng, S. Griffies, and S. Ray, 2018: Improved simulations of tropical Pacific
877 annual-mean climate in the GFDL FLOR and HiFLOR coupled GCMs. *J. Adv. Model. Earth Syst.*,
878 **10**, 3176-3220, doi:10.1029/2018MS001372.

879
880 Xiang, B., S.-J. Lin, M. Zhao, N. C. Johnson, X. Yang, and X. Jiang, 2019: Subseasonal Week 3–
881 5 Surface Air Temperature Prediction During Boreal Wintertime in a GFDL Model. *Geophys. Res.*
882 *Lett.*, **46**, 416-425, doi:[10.1029/2018GL081314](https://doi.org/10.1029/2018GL081314).

883
884 Xiang, B., S.-J. Lin, M. Zhao, S. Zhang, G. Vecchi, T. Li, X. Jiang, L. Harris, and J.-H. Chen,
885 2014: Beyond Weather Time-Scale Prediction for Hurricane Sandy and Super Typhoon Haiyan in
886 a Global Climate Model. *Mon. Weather Rev.*, **143**, 524-535.

887

888 Xu, Z., P. Chang, I. Richter, W. Kim, and G. Tang, 2014: Diagnosing southeast tropical Atlantic
889 SST and ocean circulation biases in the CMIP5 ensemble. *Clim. Dyn.*, **43**, 3123-3145,
890 doi:10.1007/s00382-014-2247-9.

891

892 Yang, X., and Coauthors, 2015: Seasonal predictability of extratropical storm tracks in GFDL's
893 high-resolution climate prediction model. *J. Climate*, **28**, 3592-3611, doi:10.1175/JCLI-D-14-
894 00517.1.

895

896 Yang, Z., and Coauthors, 2018: On the seasonal prediction of the western United States El Niño
897 precipitation pattern during the 2015/16 winter. In Press at *Clim. Dyn.*, doi:10.1007/s00382-018-
898 4109-3.

899

900 Zhang, L., C. Wang, Z. Song, and S.-K. Lee, 2014: Remote effect of the model cold bias in the
901 tropical North Atlantic on the warm bias in the tropical southeastern Pacific. *J. Adv. Model. Earth*
902 *Sys.*, **6**, 1016-1026, doi:10.1002/2014MS000338.

903

904 Zhang, L., and C. Zhao, 2014: Processes and mechanisms for the model SST biases in the North
905 Atlantic and North Pacific: A link with the Atlantic meridional overturning circulation. *J. Adv.*
906 *Model. Earth Syst.*, **7**, 739-758, doi:10.1002/2014MS000415.

907

908 Zhang, R., and T. L. Delworth, 2005: Simulated tropical response to a substantial weakening of
909 the Atlantic thermohaline circulation. *J. Climate*, **18**, 1853-1860, doi:10.1175/JCLI3460.1.

910

911 Zhang, R., and T. L. Delworth, 2007: Impact of the Atlantic Multidecadal Oscillation on the North
912 Pacific climate variability. *Geophys. Res. Lett.*, **34**, L23708, doi:10.1029/2007GL031601.

913

914 Zuidema, P. and Co-authors, 2016: Challenges and prospects for reducing coupled climate model
915 SST biases in the eastern tropical Atlantic and Pacific Oceans: The U.S. CLIVAR Eastern Tropical
916 Oceans Synthesis Working Group.. *Bull. Amer. Meteor. Soc.*, **97**, 2305–
917 2328, <https://doi.org/10.1175/BAMS-D-15-00274.1>.

918

919 **List of Figures**

920 FIG. 1. Climatological (1951-2010) annual precipitation (mm d^{-1}) in (a) observations, (b) FLOR,
921 and (c) FLOR-FA.

922

923 FIG. 2. Climatological (1951-2010) annual SST biases (K) in (a) FLOR and (b) FLOR-FA.

924

925 FIG. 3. Regions for which SSTs are restored to FA values (dark red) in (a) TPNP, (b) TANA, (c)
926 TP, and (d) TA experiments. The regions in which the color smoothly transitions from red to blue
927 indicate the buffer regions where the restoring is relaxed to zero.

928

929 FIG. 4. CTL minus FA climatological precipitation differences (mm d^{-1}) for (a,c) October – March
930 and (b,d) April – September. The top panels are the actual differences and bottom panels are
931 derived from the budget decomposition estimated from (1).

932

933 FIG. 5. Climatological precipitation biases (% relative to U. Delaware precipitation) over North
934 America in (top) FLOR and (bottom) FLOR-FA for (a,c) October – March and (b,d) April –
935 September. The values in the lower right corner of each panel are the RMSE (mm d^{-1}) in the U.S.
936 region (red box in a).

937

938 FIG. 6. FIG. 6. Impact of (left) October – March and (right) April – September (top) global,
939 (middle) tropical and extratropical Pacific, and (bottom) tropical and extratropical Atlantic FLOR
940 SST biases, including the effects of remotely induced SST biases, as expressed by the (a,b) CTL
941 minus FA, (c,d) CTL minus TPNP, and (e,f) CTL minus TANA climatological differences in
942 precipitation (color shading), SLP (contours), and 925 hPa wind (vectors) for (left) October –
943 March and (right) April – September. Precipitation differences are expressed as percentage
944 relative to CTL climatology. SLP is contoured at intervals of 1 hPa with red (blue) lines indicating
945 positive (negative) differences, and the zero contour is omitted. The reference vector for 925 hPa
946 wind is shown in the bottom right of panel d.

947

948 FIG. 7. Percent of $\delta P_{\text{FLOR-FA}}$ that can be attributed to (a,b) TPNP and (c,d) TANA domain SST
949 differences for (left) October – March and (right) April – September. Areas masked in grey
950 represent regions where the FLOR-CTL minus FLOR-FA precipitation differences are less than
951 10% of the FLOR-CTL climatological precipitation.

952

953 FIG. 8. Impact of (top) tropical Pacific and (bottom) tropical Atlantic FLOR SST biases, including
954 the effects of remotely induced SST biases, as expressed by the (a,b) CTL minus TP and (c,d) CTL
955 minus TA climatological differences in precipitation (color shading), SLP (contours), and 925 hPa

956 wind (vectors) for (left) October – March and (right) April – September. Precipitation differences
957 are expressed as percentage relative to CTL climatology. SLP is contoured at intervals of 1 hPa
958 with red (blue) lines indicating positive (negative) differences, and the zero contour is omitted.
959 The reference vector for 925 hPa wind is shown in the bottom right of panel b.

960

961 FIG. 9. (a) CTL minus TPNA and (b) CTL minus TANA annual mean climatological SST
962 differences (K).

963

964 FIG. 10. As in Fig. 8 except for the (a,b) locally forced tropical and extratropical North Atlantic
965 SST effect (CTL minus $TANA_{iso}$) and the (c,d) remotely forced tropical and extratropical North
966 Atlantic SST effect ($TANA_{iso}$ minus TANA).

967

968 FIG. 11. As in Fig. 8 except for the (a,b) locally forced tropical and extratropical North Pacific
969 SST effect (CTL minus $TPNP_{iso}$) and the (c,d) remotely forced tropical and extratropical North
970 Pacific SST effect ($TPNP_{iso}$ minus TPNP).

971

972 FIG. 12. Contributions to the October – March (left column) CTL minus FA, (middle column)
973 CTL minus TPNP, and (right column) CTL minus TANA climatological precipitation
974 differences (mm d^{-1}) attributed to the following terms: (a-c) circulation bias, (d-f) humidity bias,
975 (g-i) evaporation, and (j-l) the residual, calculated as the actual precipitation difference minus the
976 sum of the three terms.

977

978 FIG. 13. As in Fig. 12 but for April – September.

979

980 FIG. 14. Climatological storm tracks, as measured by 8-day high-pass filtered 500 hPa geopotential
981 height variance (shading, m^2) and 200 hPa zonal wind (grey contours at an interval of 10 ms^{-1}) for
982 (left) NCEP/NCAR reanalysis data, (center) FA, and (right) CTL simulations in (a-c) October –
983 March and (d-f) April – September.

984

985 FIG. 15. Differences in climatological storm tracks, as measured by 8-day high-pass filtered 500
986 hPa geopotential height variance (shading, m^2), and 200 hPa zonal wind (grey contours at an
987 interval of 2 ms^{-1} , zero contour is omitted) for (a,b) CTL minus FA, (c,d) CTL minus TPNP, and
988 (e,f) CTL minus TANA in (left) October – March and (right) April – September.

989

990 FIG. 16. Schematic showing the dominant impacts of Pacific and Atlantic SST biases on North
991 American precipitation biases in the boreal cold and warm seasons. In the boreal cold season, (a)
992 negative SST biases in the extratropical North Pacific promote a strengthened and southerly shifted
993 storm track, which enhances precipitation in the southwestern United States and suppresses
994 precipitation in northern Canada. (b) Tropical Atlantic cold SST biases induce circulation changes
995 throughout the entire tropics resembling the classic Gill model, with a surface anticyclone in the
996 vicinity of the cold bias and low-level convergence and enhanced precipitation in the equatorial
997 Pacific. The enhanced tropical Pacific rainfall excites a deepened Aleutian low and enhanced
998 moisture transport and precipitation in the southern United States. In the boreal warm season, the
999 effects of (c) North Pacific SST biases are modest, but a weaker northern portion of the North
1000 Pacific storm track promotes drier conditions in northern North America. (d) The cold Atlantic
1001 SST biases have a much stronger impact, substantially strengthening the western lobe of the North

1002 Atlantic Subtropical High and weakening the thermal low over southern North America. These
1003 changes enhance the Great Plains Low Level jet and moisture transport into southwestern North
1004 America. Because the SST biases in each basin influence the SST biases in the other basin, the
1005 total SST bias effects are not limited to the direct effects described here.

1006

1007

1008

1009

1010

1011

1012

1013

1014

1015

1016

1017

1018

1019

1020

1021

1022

1023

1024

1025 Table 1. List of FLOR experiments analyzed in this study.

Experiment name	Description	Duration (years)
CTL	FLOR with 1990 radiative forcings	100
FA	FLOR with 1990 radiative forcings and flux adjustments to correct SST biases	100
TPNP	CTL but with tropical and extratropical North Pacific SSTs restored to FA values	100
TANA	CTL but with tropical and extratropical North Atlantic SSTs restored to FA values	100
TP	CTL but with tropical Pacific SSTs restored to FA values	100
TA	CTL but with tropical Atlantic SSTs restored to FA values	100
TPNP _{iso}	As in TPNP but with tropical and extratropical North Atlantic SSTs restored to CTL values	50
TANA _{iso}	As in TANA but with tropical and extratropical North Pacific SSTs restored to CTL values	50

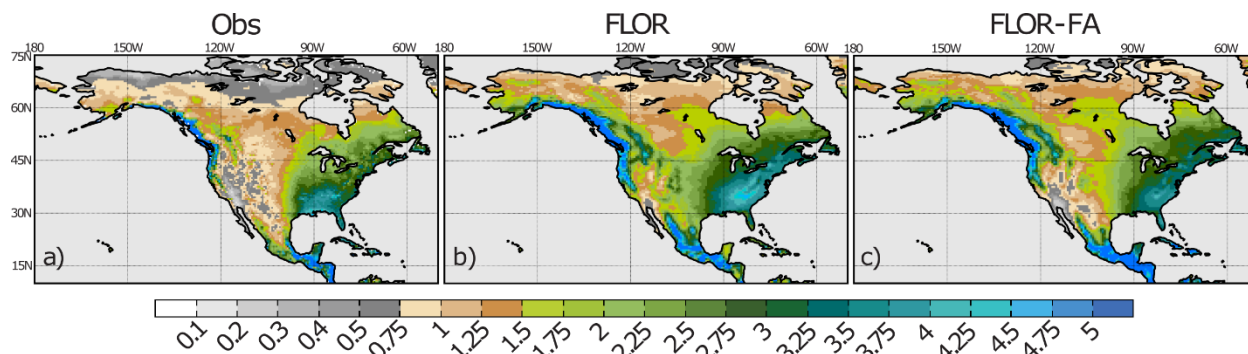
1026

1027

1028

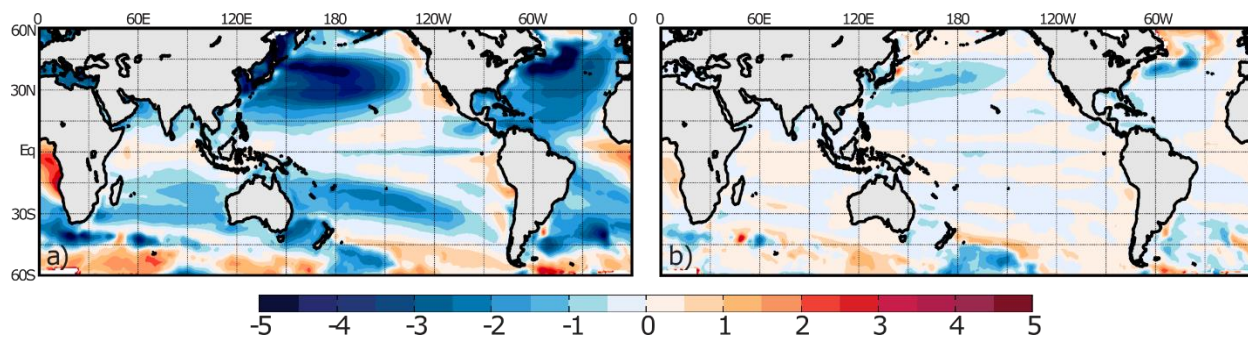
1029

1030



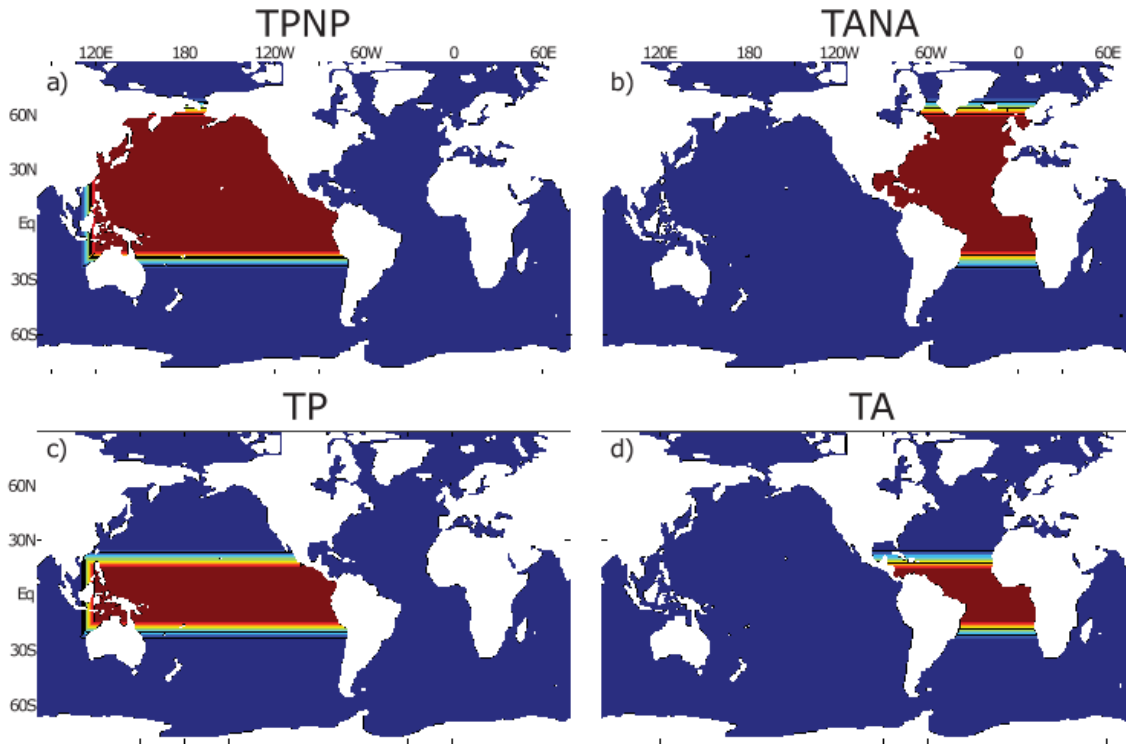
1031
 1032 FIG. 1. Climatological (1951-2010) annual precipitation (mm d^{-1}) in (a) observations, (b) FLOR,
 1033 and (c) FLOR-FA.

1034
 1035
 1036
 1037



1038
 1039
 1040 FIG. 2. Climatological (1951-2010) annual SST biases (K) in (a) FLOR and (b) FLOR-FA.

1041
 1042



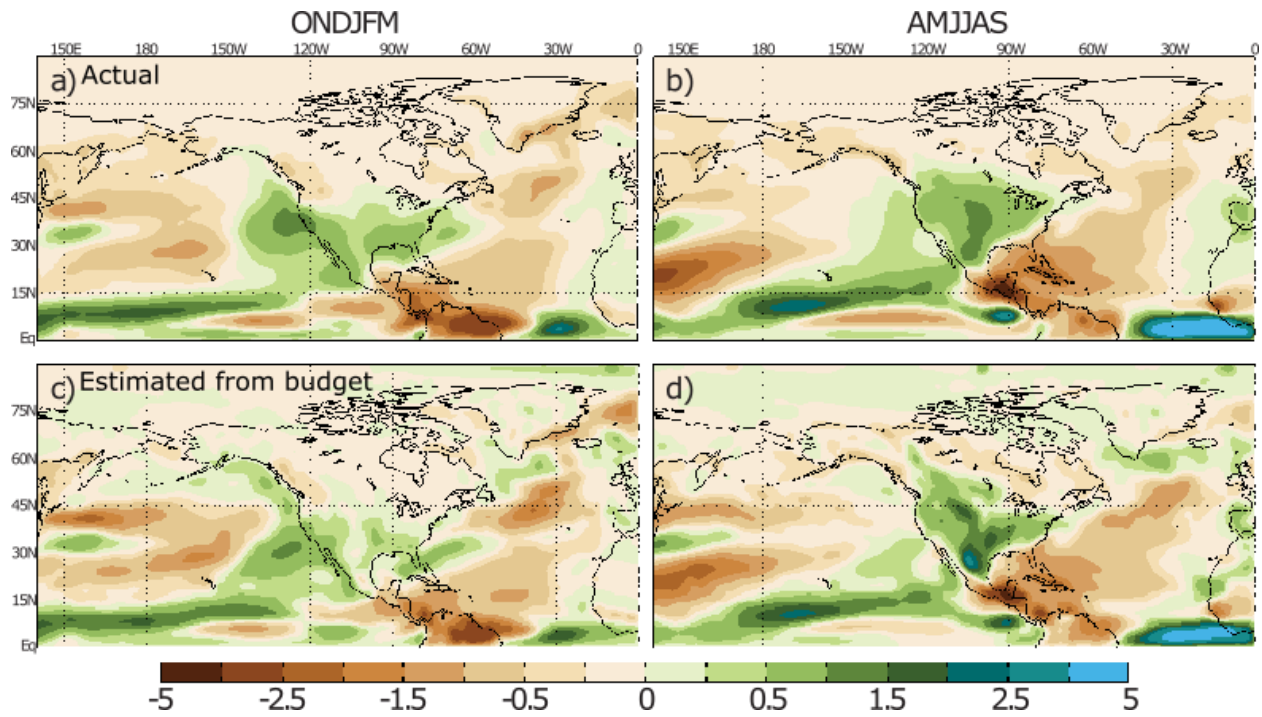
1043

1044 FIG. 3. Regions for which SSTs are restored to FA values (dark red) in (a) TPNP, (b) TANA, (c)
 1045 TP, and (d) TA experiments. The regions in which the color smoothly transitions from red to blue
 1046 indicate the buffer regions where the restoring is relaxed to zero.

1047

1048

1049



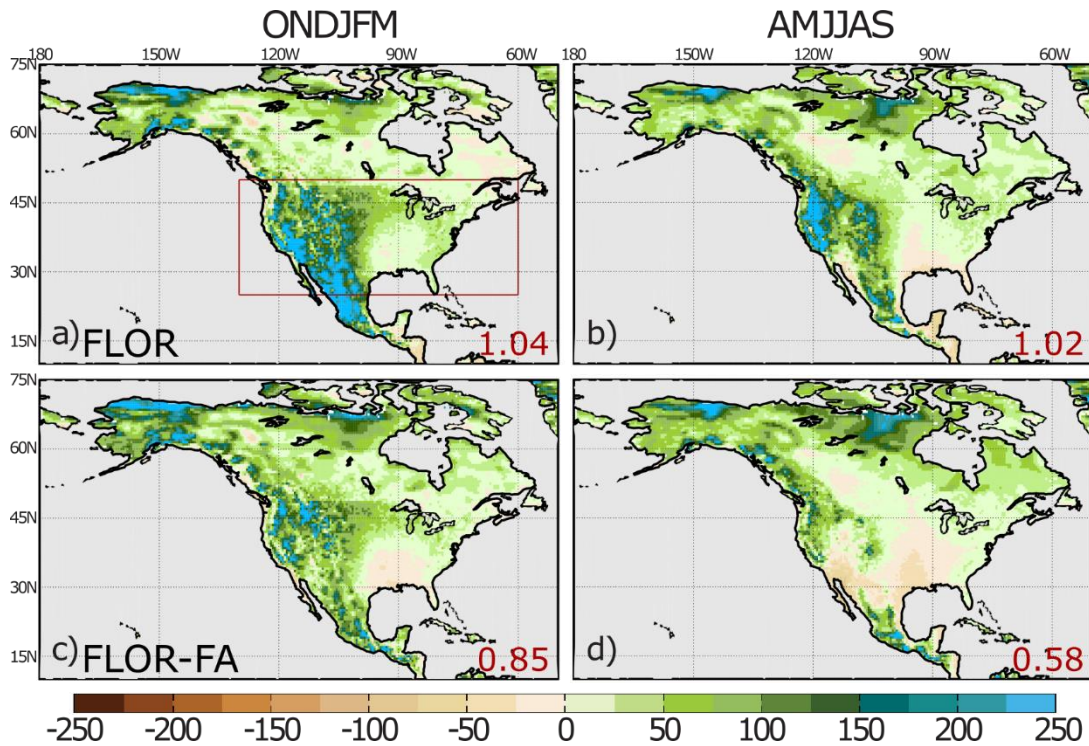
1050
 1051
 1052 FIG. 4. CTL minus FA climatological precipitation differences (mm d^{-1}) for (a,c) October – March
 1053 and (b,d) April – September. The top panels are the actual differences and bottom panels are
 1054 derived from the budget decomposition estimated from (1).

1055

1056

1057

1058



1059

1060 FIG. 5. Climatological precipitation biases (% relative to U. Delaware precipitation) over North
 1061 America in (top) FLOR and (bottom) FLOR-FA for (a,c) October – March and (b,d) April –
 1062 September. The values in the lower right corner of each panel are the RMSE (mm d^{-1}) in the U.S.
 1063 region (red box in a).

1064

1065

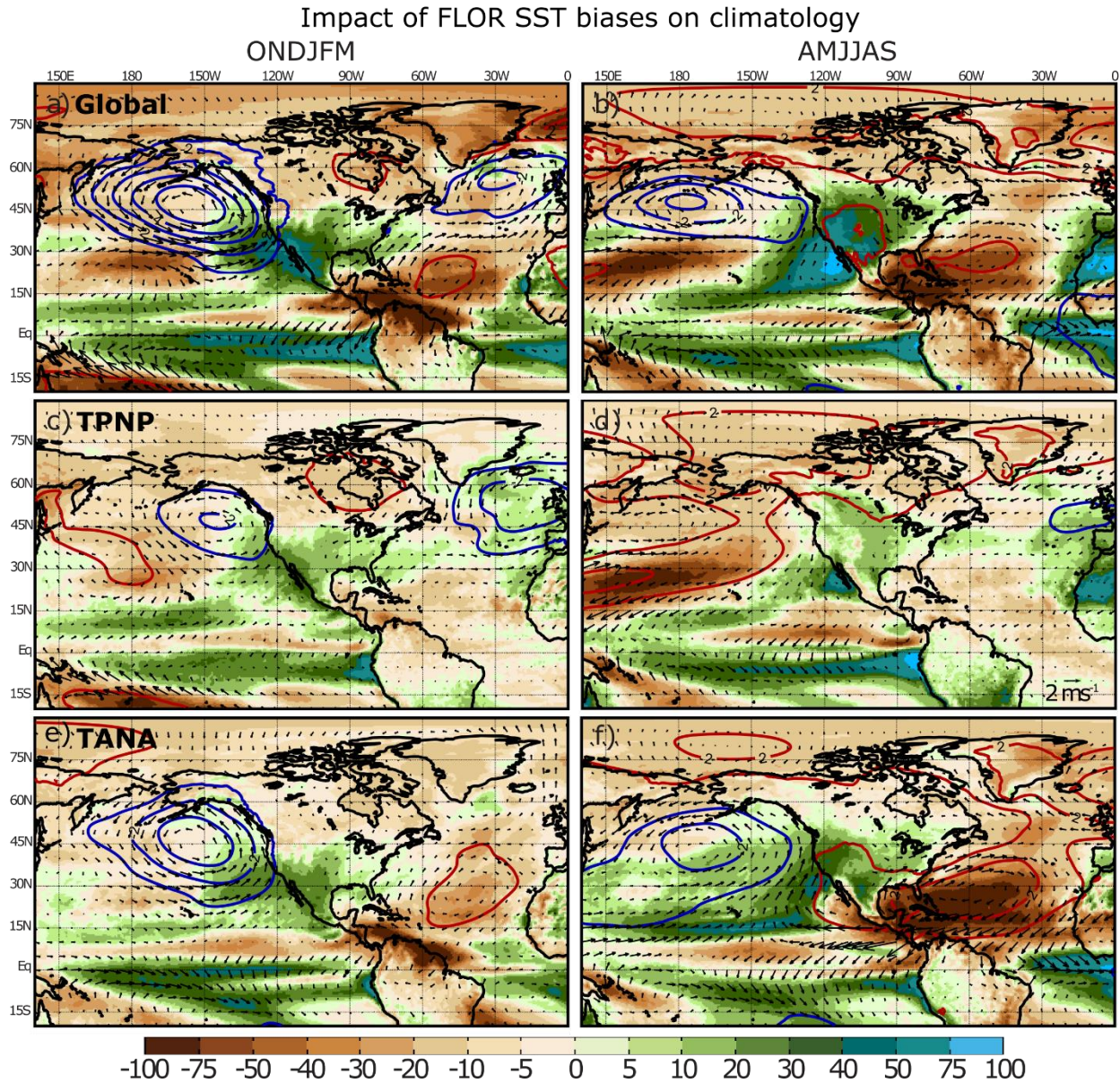
1066

1067

1068

1069

1070



1071

1072 FIG. 6. Impact of (left) October – March and (right) April – September (top) global, (middle)

1073 tropical and extratropical Pacific, and (bottom) tropical and extratropical Atlantic FLOR SST

1074 biases, including the effects of remotely induced SST biases, as expressed by the (a,b) CTL minus

1075 FA, (c,d) CTL minus TPNP, and (e,f) CTL minus TANA climatological differences in

1076 precipitation (color shading), SLP (contours), and 925 hPa wind (vectors) for (left) October –

1077 March and (right) April – September. Precipitation differences are expressed as percentage

1078 relative to CTL climatology. SLP is contoured at intervals of 1 hPa with red (blue) lines indicating

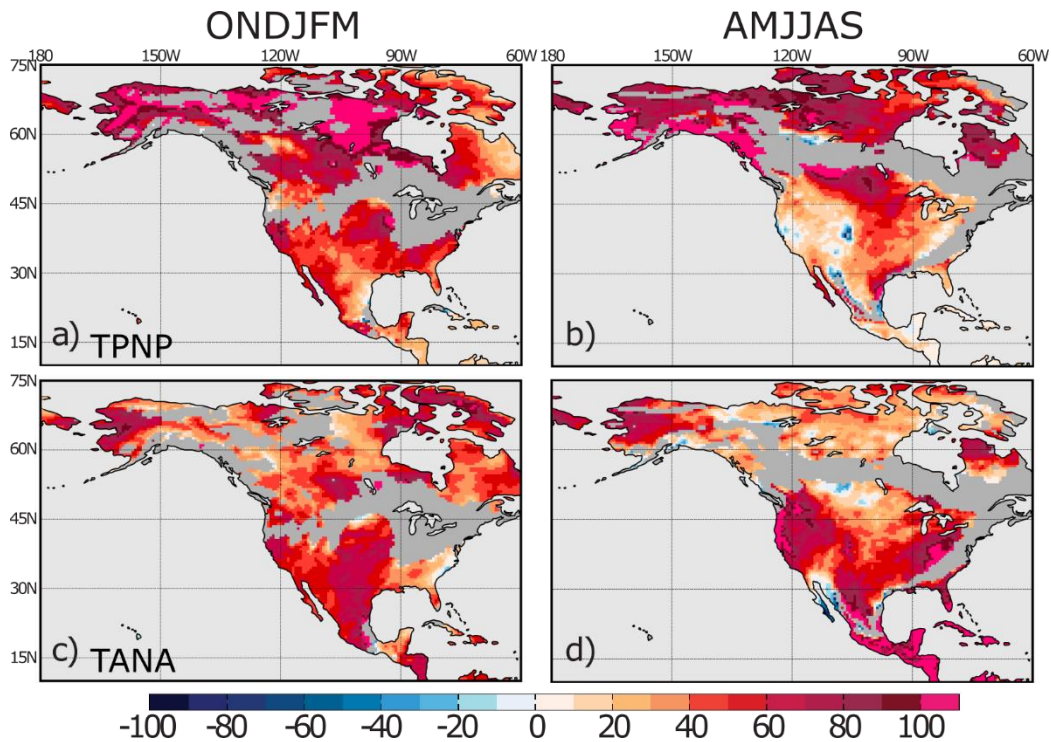
1079 positive (negative) differences, and the zero contour is omitted. The reference vector for 925 hPa
1080 wind is shown in the bottom right of panel d.

1081

1082

1083

1084



1085

1086

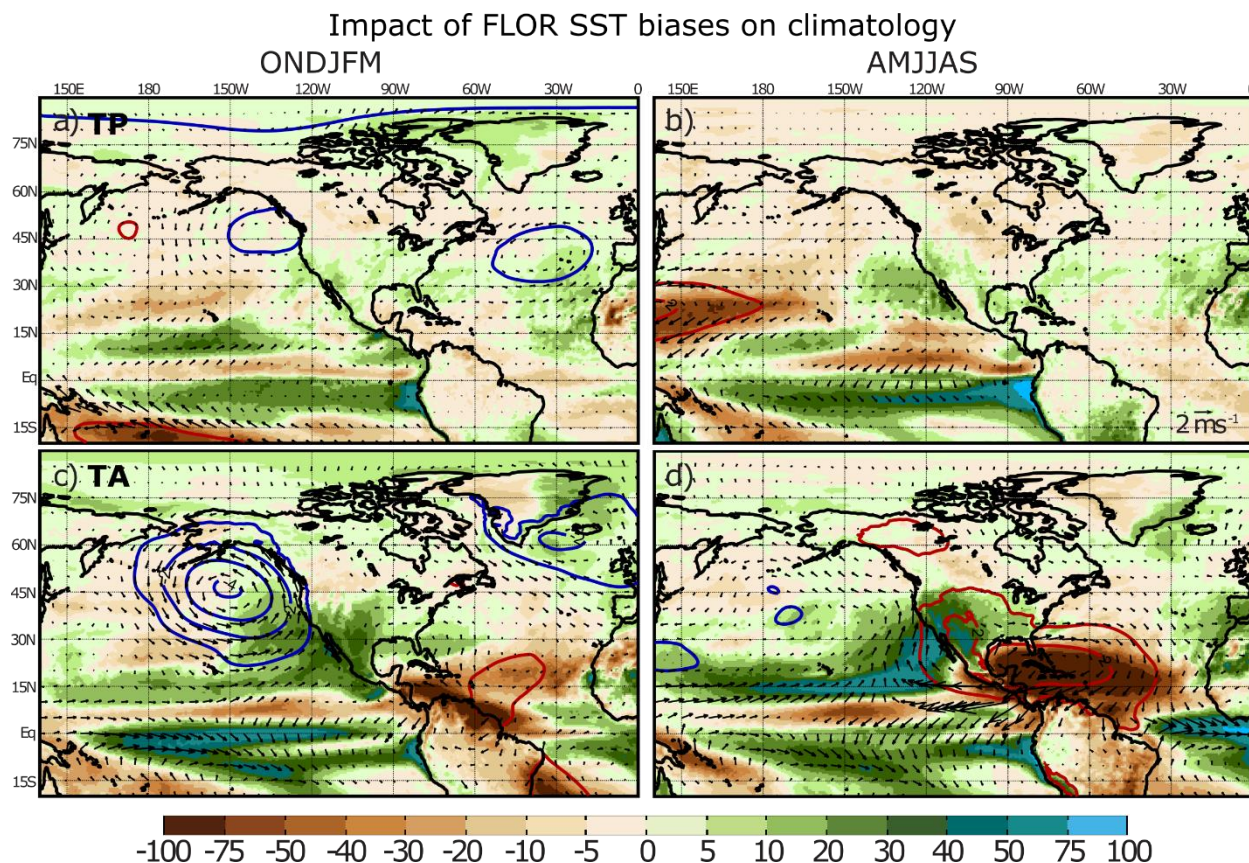
1087 FIG. 7. Percent of $\delta P_{\text{FLOR-FA}}$ that can be attributed to (a,b) TPNP and (c,d) TANA domain SST
1088 differences for (left) October – March and (right) April – September. Areas masked in grey
1089 represent regions where the FLOR-CTL minus FLOR-FA precipitation differences are less than
1090 10% of the FLOR-CTL climatological precipitation.

1091

1092

1093

1094



1095

1096 FIG. 8. Impact of (top) tropical Pacific and (bottom) tropical Atlantic FLOR SST biases, including

1097 the effects of remotely induced SST biases, as expressed by the (a,b) CTL minus TP and (c,d) CTL

1098 minus TA climatological differences in precipitation (color shading), SLP (contours), and 925 hPa

1099 wind (vectors) for (left) October – March and (right) April – September. Precipitation differences

1100 are expressed as percentage relative to CTL climatology. SLP is contoured at intervals of 1 hPa

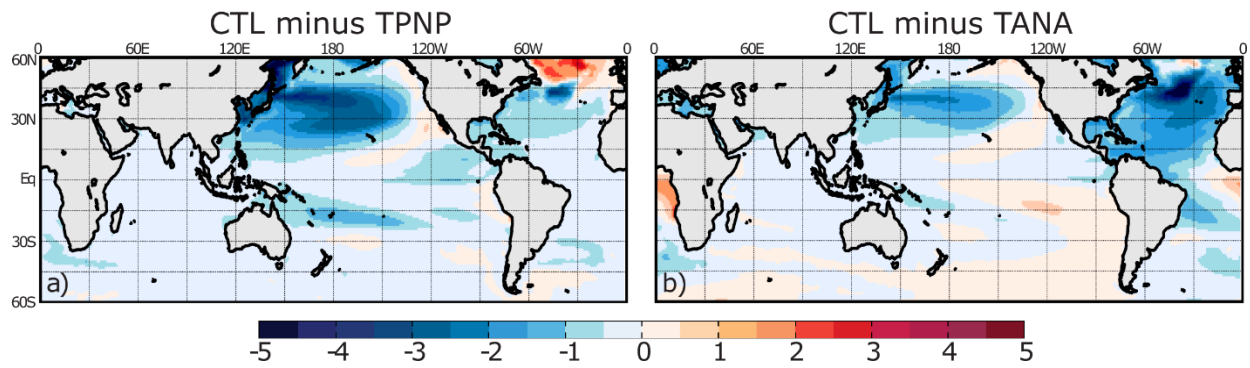
1101 with red (blue) lines indicating positive (negative) differences, and the zero contour is omitted.

1102 The reference vector for 925 hPa wind is shown in the bottom right of panel b.

1103

1104

1105



1106

1107 FIG. 9. (a) CTL minus TPNP and (b) CTL minus TANA annual mean climatological SST
1108 differences (K).

1109

1110

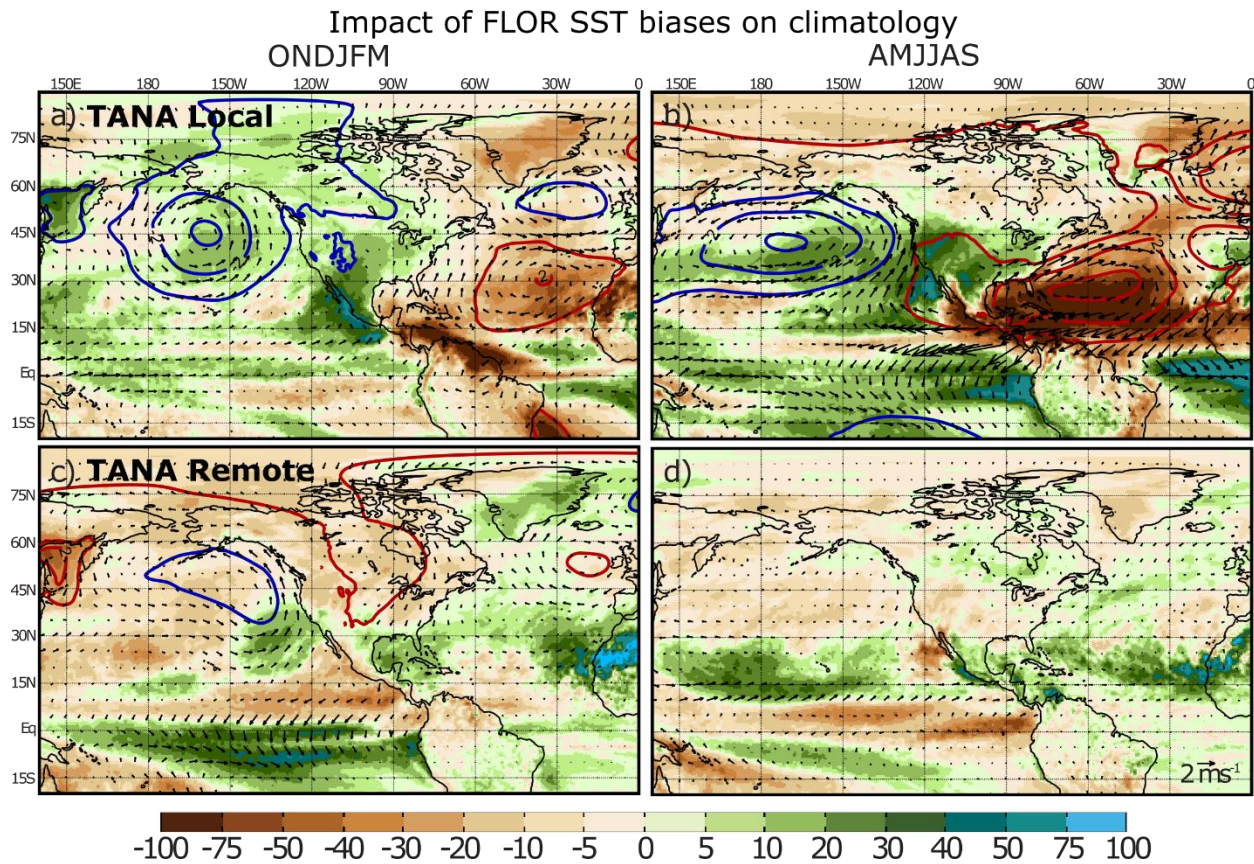
1111

1112

1113

1114

1115



1116

1117 FIG. 10. As in Fig. 8 except for the (a,b) locally forced tropical and extratropical North Atlantic

1118 SST effect (CTL minus $TANA_{iso}$) and the (c,d) remotely forced tropical and extratropical North

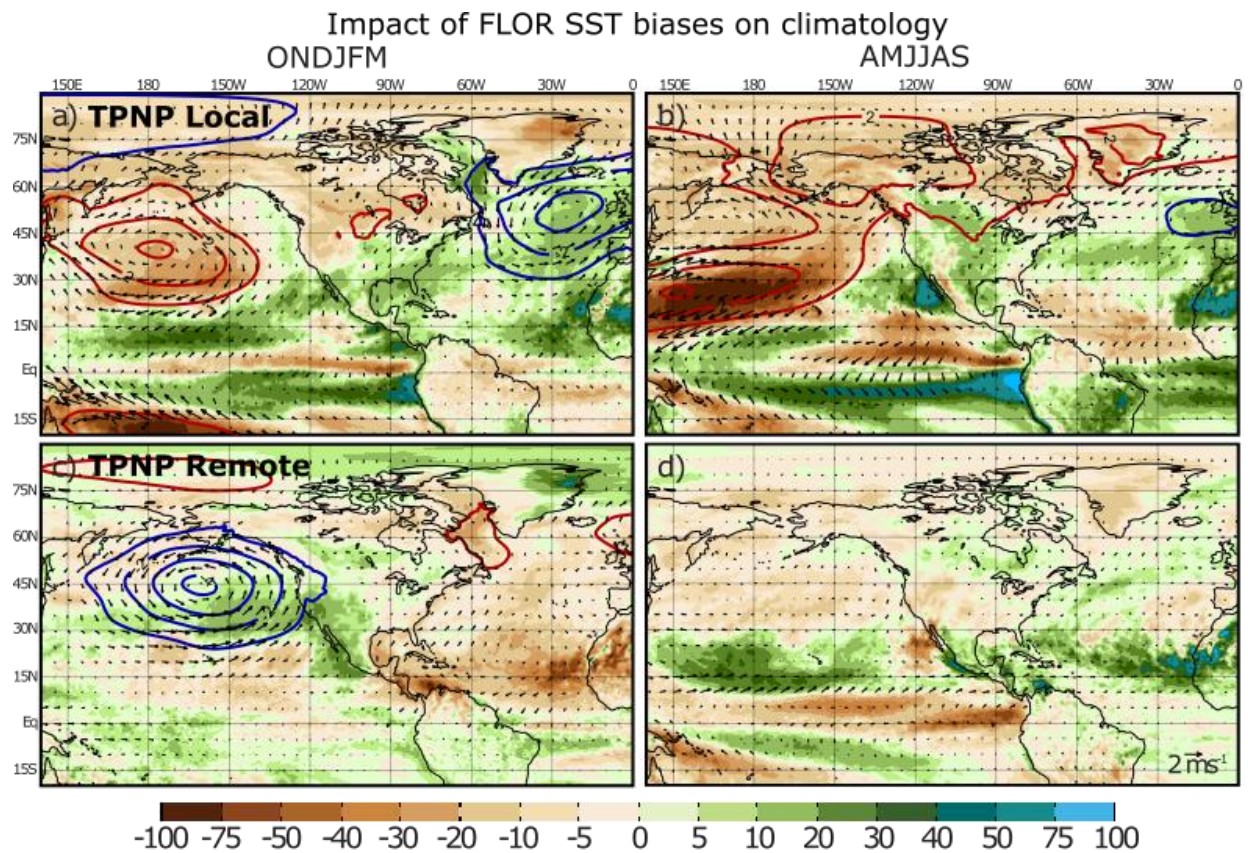
1119 Atlantic SST effect ($TANA_{iso}$ minus TANA).

1120

1121

1122

1123



1124

1125 FIG. 11. As in Fig. 8 except for the (a,b) locally forced tropical and extratropical North Pacific

1126 SST effect (CTL minus TPNP_{iso}) and the (c,d) remotely forced tropical and extratropical North

1127 Pacific SST effect (TPNP_{iso} minus TPNP).

1128

1129

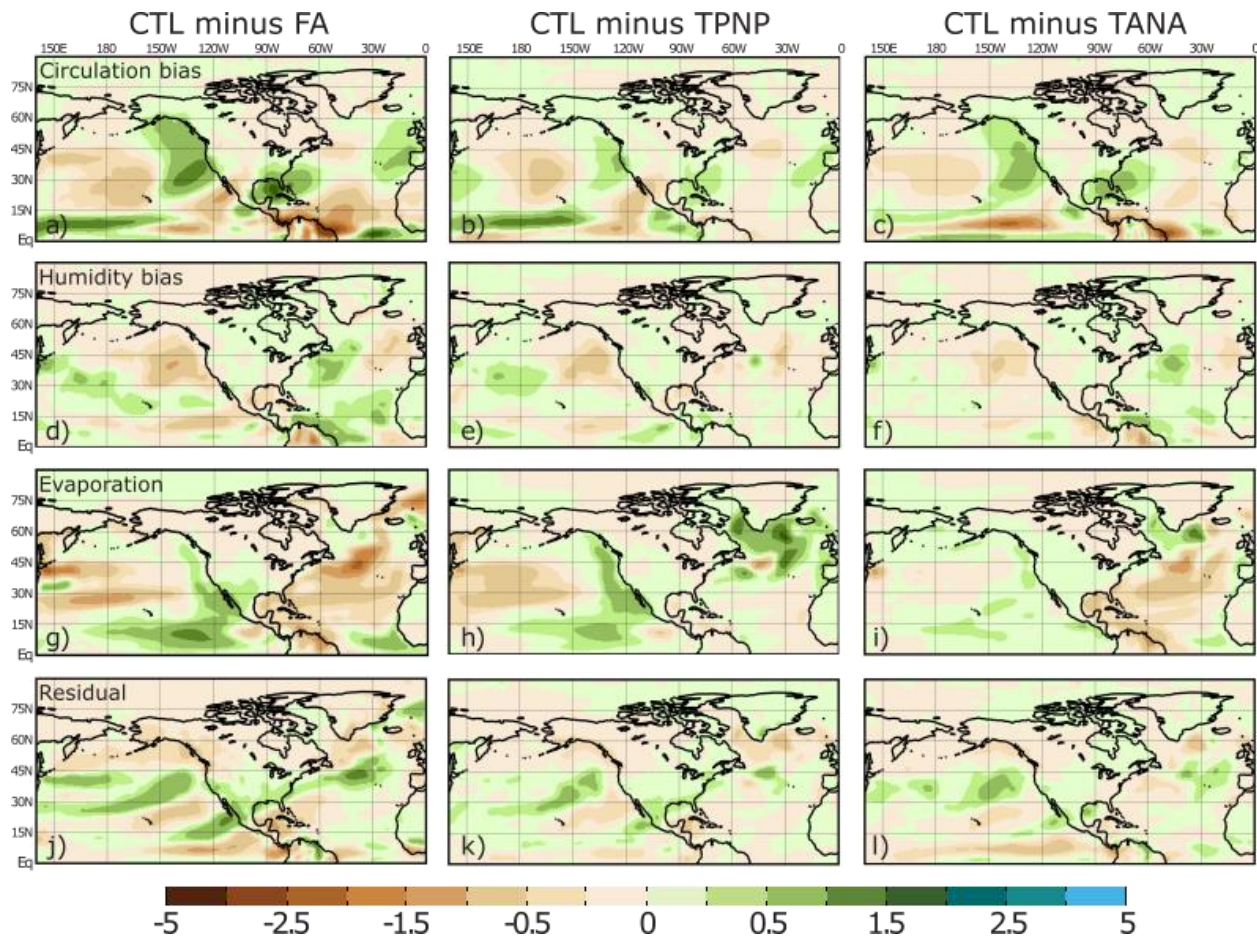
1130

1131

1132

1133

1134



1135
 1136 FIG. 12. Contributions to the October – March (left column) CTL minus FA, (middle column)
 1137 CTL minus TPNP, and (right column) CTL minus TANA climatological precipitation
 1138 differences (mm d^{-1}) attributed to the following terms: (a-c) circulation bias, (d-f) humidity bias,
 1139 (g-i) evaporation, and (j-l) the residual, calculated as the actual precipitation difference minus the
 1140 sum of the three terms.

1141

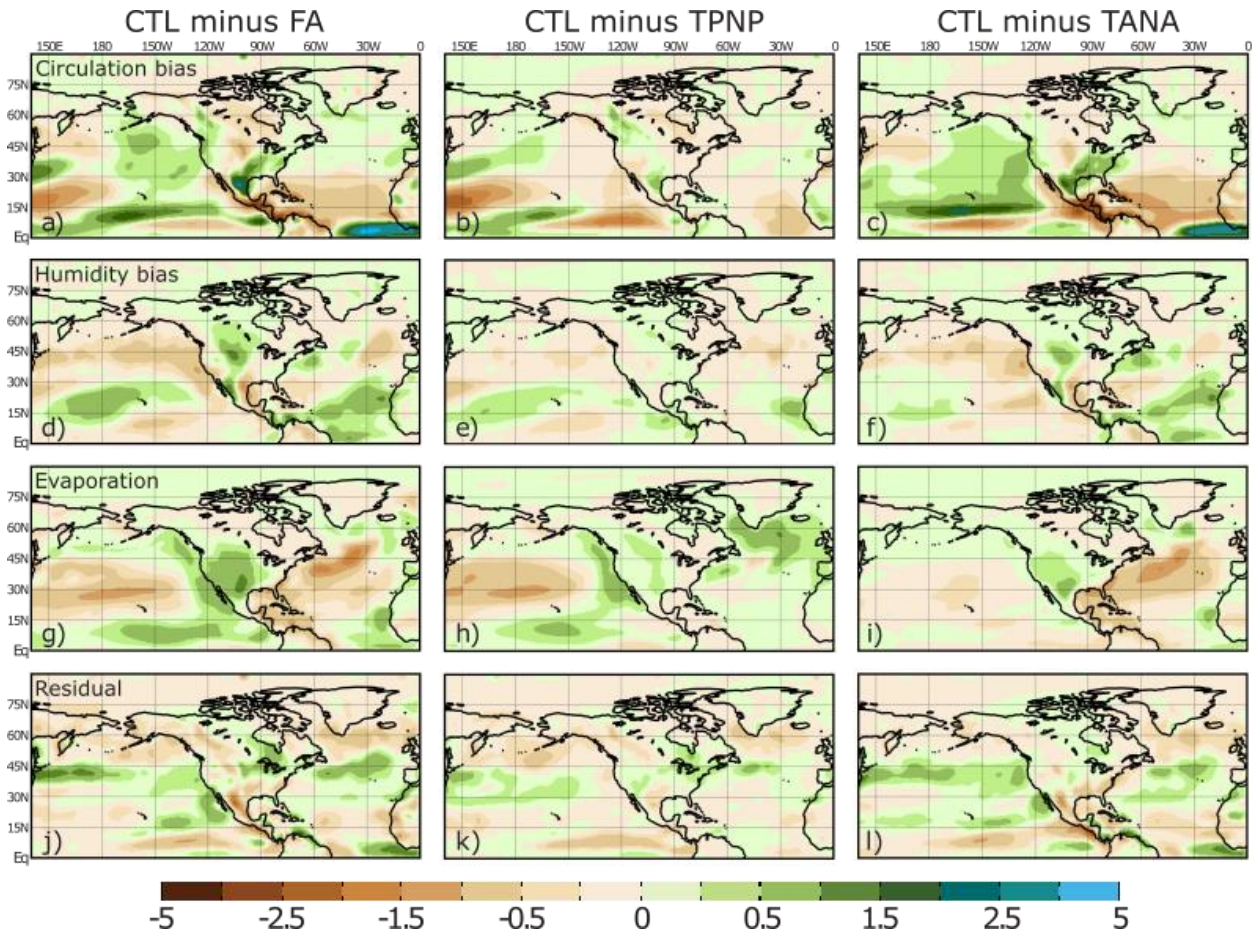
1142

1143

1144

1145

1146



1147

1148 FIG. 13. As in Fig. 12 but for April – September.

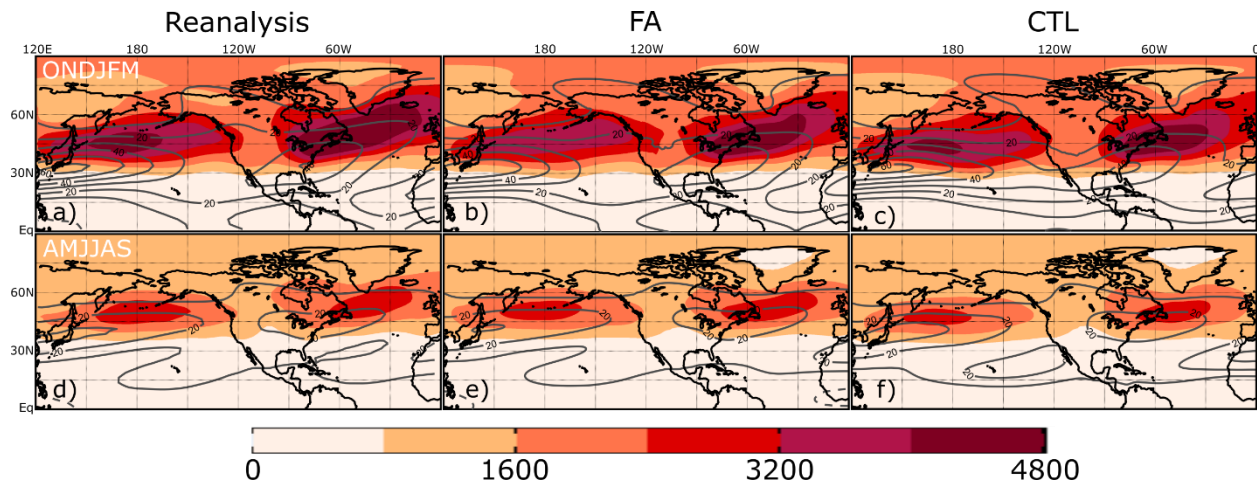
1149

1150

1151

1152

1153



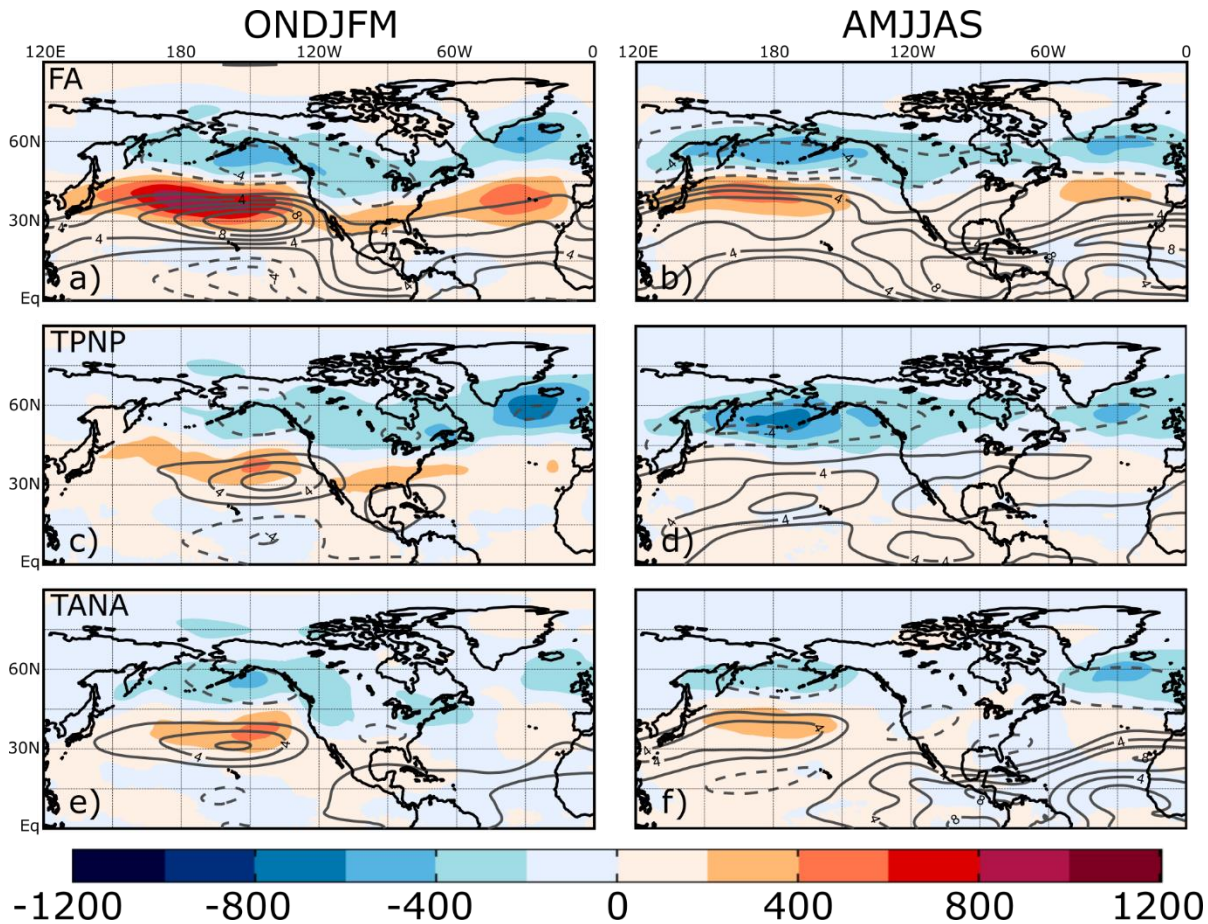
1154

1155 FIG. 14. Climatological storm tracks, as measured by 8-day high-pass filtered 500 hPa geopotential
 1156 height variance (shading, m^2) and 200 hPa zonal wind (grey contours at an interval of 10 ms^{-1}) for
 1157 (left) NCEP/NCAR reanalysis data, (center) FA, and (right) CTL simulations in (a-c) October –
 1158 March and (d-f) April – September.

1159

1160

1161



1162 -1200 -800 -400 0 400 800 1200

1163 FIG. 15. Differences in climatological storm tracks, as measured by 8-day high-pass filtered 500

1164 hPa geopotential height variance (shading, m^2), and 200 hPa zonal wind (grey contours at an

1165 interval of 2 ms^{-1} , zero contour is omitted) for (a,b) CTL minus FA, (c,d) CTL minus TPNP, and

1166 (e,f) CTL minus TANA in (left) October – March and (right) April - September.

1167

1168

1169

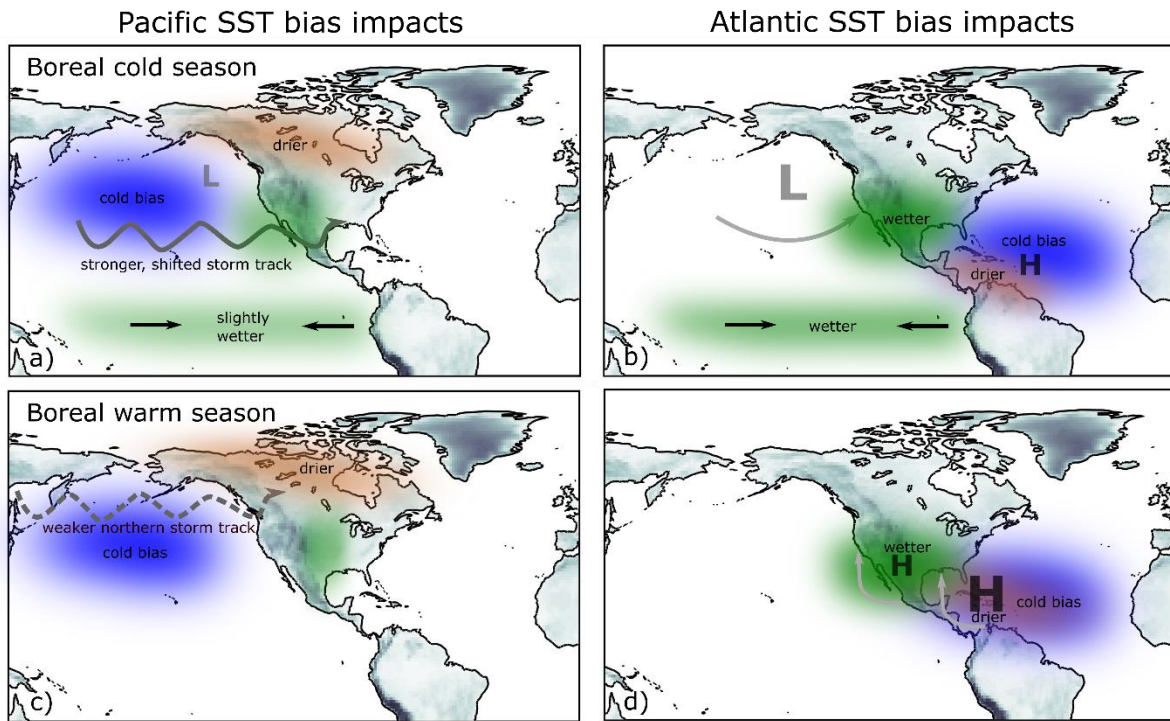
1170

1171

1172

1173

1174



1175

1176 FIG. 16. Schematic showing the dominant impacts of Pacific and Atlantic SST biases on North
1177 American precipitation biases in the boreal cold and warm seasons. In the boreal cold season, (a)
1178 negative SST biases in the extratropical North Pacific promote a strengthened and southerly shifted
1179 storm track, which enhances precipitation in the southwestern United States and suppresses
1180 precipitation in northern Canada. (b) Tropical Atlantic cold SST biases induce circulation changes
1181 throughout the entire tropics resembling the classic Gill model, with a surface anticyclone in the
1182 vicinity of the cold bias and low-level convergence and enhanced precipitation in the equatorial
1183 Pacific. The enhanced tropical Pacific rainfall excites a deepened Aleutian low and enhanced
1184 moisture transport and precipitation in the southern United States. In the boreal warm season, the
1185 effects of (c) North Pacific SST biases are modest, but a weaker northern portion of the North
1186 Pacific storm track promotes drier conditions in northern North America. (d) The cold Atlantic
1187 SST biases have a much stronger impact, substantially strengthening the western lobe of the North

1188 Atlantic Subtropical High and weakening the thermal low over southern North America. These
1189 changes enhance the Great Plains low-level jet and moisture transport into southwestern North
1190 America. Because the SST biases in each basin influence the SST biases in the other basin, the
1191 total SST bias effects are not limited to the direct effects described here.